Decoupling Motion from Sensory Data:
An Emergent Property of a Neural Population in the Piriform Cortex

Doctoral program in ‘Cognitive and Brain Sciences’
PhD Candidate, Filippo Michelon
Supervisor, Giuliano Iurilli

CiMeC
Center for Mind/Brain Sciences

University of Trento
XXXVI Cycle
Academic Year 2020-2024

iit SyNe
ISTITUTO ITALIANO
DI TECNOLOGIA
SYSTEMS NEUROBIOLOGY

Acknowledgements

I would like to express my thanks to my family for their support throughout this journey. To all my friends, your encouragement and companionship have been invaluable. My deepest gratitude goes to my supervisor and lab colleagues, past and present, for their collaboration, support and friendship. Finally, I am grateful to everyone who contributed to the completion of this thesis. Thank you all.

Ringraziamenti

Desidero esprimere il mio più sentito ringraziamento alla mia famiglia per il loro sostegno durante questo percorso. A tutti i miei amici, il vostro incoraggiamento e la vostra compagnia sono stati inestimabili. Un grazie di cuore al mio supervisore e ai miei colleghi di laboratorio, presenti e passati, per la collaborazione, il sostegno e l'amicizia. Infine, sono grato a tutti coloro che hanno contribuito al completamento di questa tesi. Grazie a tutti.

Source acknowledgment

The data showed in this thesis are published in Cell Reports Journal: A. Dehaqani, A., Michelon, F., Patella, P., Petrucco, L., Piasini, E., Iurilli, G., 2024. A mechanosensory feedback that uncouples external and self-generated sensory responses in the olfactory cortex. Cell Reports 43, 114013. Copyright Elsevier ©.
DOI: https://doi.org/10.1016/j.celrep.2024.114013

Abstract

Modulation of breathing rate is crucial to flexibly explore the olfactory environment. Inhalation gates the perception of scents, and the act of sniffing is necessary for the olfactory percept. In olfaction, sniffing increases the airflow velocity inside the nostrils and the number of odor molecules that contact the olfactory epithelium during each inhalation. Yet, animals can discriminate odor concentration regardless of the velocity of their inhalation. Sniffing and regular breathing differently influence the activity of the olfactory cortex during a single inhalation. Still, the population representation of odor concentration is invariant to fluctuations in the breathing rate. This can be explained by the fact that inhalation speed and odor concentration responses are uncorrelated within and across neurons in the piriform cortex. Thanks to this feature, a faster odor inhalation and an increase in concentration change the cortical activity pattern in distinct ways. This encoding strategy may represent a broader principle by which the brain maintains perceptual stability against the sensory perturbations introduced by active sampling behaviors.

Index

Introduction

Respiratory signals in the brain

If you try to hold your breath over a jar of freshly ground coffee, you will notice (not so surprisingly) that you are unable to sense any smell; however, even just a small inhalation on top of the jar is enough to start a perceptive aromatic explosion. We experience the power of holding our breath, for instance, when we try to escape an unpleasant smell at the wrong street corner in the city center. On the other hand, we almost unconsciously take deeper and faster breaths when we encounter the inviting scent of baked bread on the street. These everyday life examples tell a lot about the tight bond between olfactory perception and respiration.

The scientific literature that describes the relationship between respiratory signals and the olfactory dimension goes back to 1942, when Edgar Douglas Adrian, a British electrophysiologist, was the first to report that: "*the olfactory organ can be stimulated mechanically by the air current as well as chemically by the odours in it*." He performed some of the first electrophysiological recordings in the piriform lobes, showing that electric activity oscillates at the frequences of respiration even in the absence of odors (Figure 1); moreover, he was also able to induce such oscillations in tracheotomized hedgehogs with artificial protocols of air stimulations (Adrian, 1942).

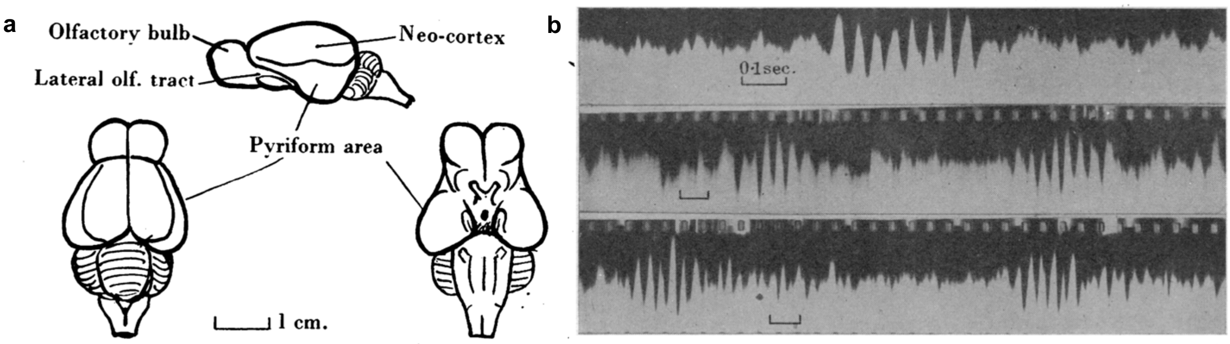

Figure 1. Nasal airflow activates the piriform lobes

(**a**) Diagram of the brain of the hedgehog. (**b**) example traces of electrophysiological recordings in the pyriform lobe of an anesthetized hedgehog breathing normal air; electric waves of the order of 0.2mW oscillate at the frequencies of respiration. Figure taken from (Adrian, 1942).

The tight dependence of olfactory perception with respiration was later demonstrated by injecting intravenously human subjects with different odorants. Such an approach allows the circulatory system to spread the odorant through the bloodstream up to the capillaries in the olfactory epithelium. As long as the subject was holding its breath, no odor was perceived, but at the start of the first breath, perception occurred, suggesting that was the coincidence of the odorant molecules at the epithelium and the airflow inside the nasal cavities that allowed for olfactory sensory perception (Bocca et al., 1965). The link between respiration and olfaction was even shown to be a good biomarker for consciousness in patients with brain injuries. Sniffing features change according to the odor pleasantness in patients with disorders of consciousness. Very strikingly, if a patient showed a sniff response, this guaranteed eventual return to consciousness (Arzi et al., 2020). Studies with functional magnetic resonance imaging (fMRI) showed that the act of sniffing is not only necessary for the perception of scents but is also sufficient to observe cortical activation in the piriform cortex in the absence of odors, thanks to the airflow passage through the nasal cavity (Figure 2) (Mainland and Sobel, 2006; Sobel et al., 1998).

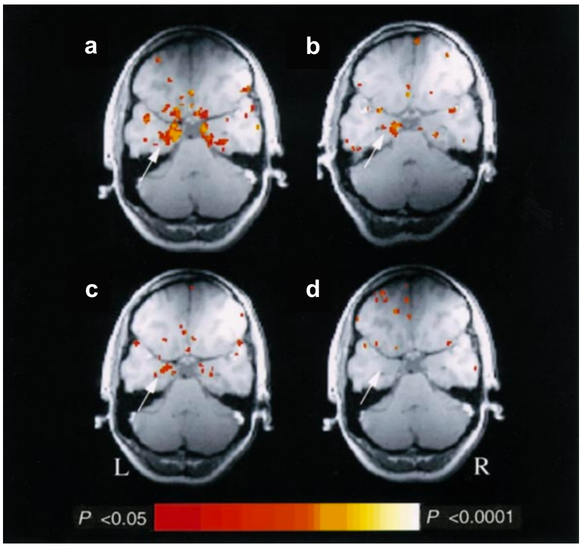

Figure 2. Nasal airflow activates the piriform cortex
(**a**) Sniffing activates the piriform cortex. (**b**) A reduction in the piriform activation is seen under anesthesia. (**c**) Subject lying passively while artificial sniffing occurs. Piriform activation is seen. (**d**) Nostrils are occluded to avoid airflow passage; the subject is trying to perform the motor action of sniffing. There is no activation of piriform cortex. All fMRI images come from the healthy subject DP. Figure taken from (Sobel et al., 1998).

Also, it has been nicely shown with intracranial electroencephalogram (EEG) data that is the actual nasal air passage through the nostrils that produces oscillations coupled with respiration in the piriform cortex, indeed when asking a subject to volitionally perform breaths through the mouth, such respiration-coupled oscillations disappeared (Zelano et al., 2016).

Respiratory signals in the brain not only affect the olfactory perception but extend even to other sensory modalities. For instance, it has been shown that human performance in a visuospatial perceptive task was improved when the subject showed a spontaneous inhalation aligned with the onset of the task. This was also mirrored by increased activity in task-related brain regions (Perl et al., 2019).

Respiration-coupled oscillations were found throughout the mouse and rat brains, too. From the olfactory bulb and piriform cortex (Fontanini et al., 2003) to the dentate gyrus, somatosensory and prefrontal cortex (Tort et al., 2018). In the prefrontal cortex, it has also been shown that in awake immobile mice, the coherence in the spectral power between local field potential and respiration at the respiratory frequencies disappears after surgical ablation of the olfactory bulbs, suggesting that, at least some brain regions, receive respiratory signals from the nasal cavities rather than from respiratory centers located in the brainstem (Tort et al., 2018). Also, the respiration-entrained activity seen in the prefrontal cortex has an impact at the behavioral level, disrupting respiratory inputs from the olfactory epithelium, for instance, prolonged freezing behaviors in mice (Moberly et al., 2018). The ubiquity of respiratory signals found in the brain suggests its involvement in multiple mechanisms; it has also been proposed that respiration-entrained rhythms might be a channel for communication between brain areas (Tort et al., 2018).

If it is true that olfactory stimuli can affect respiration to a certain degree, it is also true that olfactory perception is fully dependent on respiration. On the other side, respiration does not depend on olfaction; it serves more vital functions in terms of animal survival. The primary role of respiration is indeed to provide the oxygen needed for energy production and to remove metabolic waste products like carbon dioxide. As animals increased in size and complexity, they evolved specialized organs to exchange gases with the environment efficiently. Mammals evolved lungs, controlled by a central pattern generator circuit in the brainstem. The circuit is composed of several nuclei and has its core the preBötzinger complex. Neurons in these nuclei own rhythmogenic capabilities and control respiration via spinal and cranial motor nuclei. Chemical and mechanical receptors located in the periphery feedback relevant information to the brainstem (Figure 3) (Del Negro et al., 2018). The communication between peripheral sensors and the central nervous system is still an ongoing field of research: thanks to genetic tools, it is now possible to characterize the roles of different neurons and their specific effects on breathing. For instance, Chang et al., 2015 described the different roles of specific subpopulations of neurons in the vagal nerve, a primary communication channel between the lungs and the brain, and their involvement in specific respiratory behaviors. Respiration is not only about gas exchanges but is tightly linked with complex emotions like fear and calm states, as changes in breathing patterns can both reflect and influence these emotional states. For instance, mindfulness practices based on voluntary control over respiration were shown to alter brain states (Lutz et al., 2004). Overall, it has been shown that training to modify breathing rate and depth is a powerful and effective channel to control emotional states such as stress, depression, and anxiety (Ashhad et al., 2022).

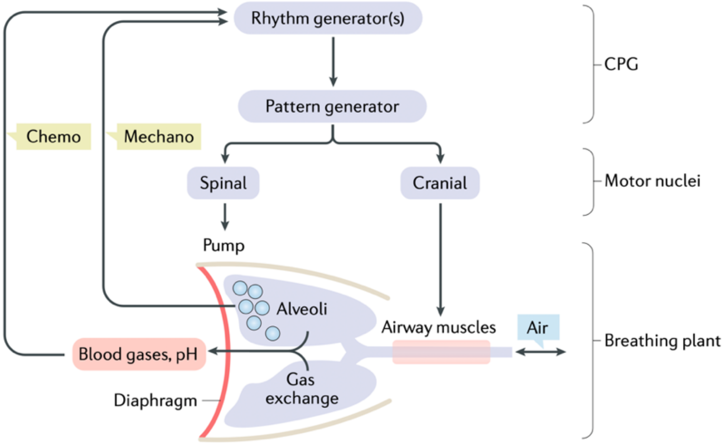

Figure 3. Schematic drawing showing respiratory circuits

The central pattern generator (CPG) controls spinal and cranial motor nuclei, which in turn innervate pump and airway muscles. A feedback loop that brings mechanical and chemical information to the CPG is shown too. Figure taken from (Del Negro et al., 2018).

As mentioned before, respiration is the carrier of olfactory perception, and it is thus not surprising that animals have developed exploratory respiratory strategies to probe the olfactory dimension of the sensory world. Unlike vision that collects distal cues from light information to drive behavior, the olfactory representation is built on two close sampling detectors (i.e., nostrils) at the tip of the snout. The sampling frequency is a key feature of every sensory organ because it lays the foundation for what can be perceivable; for example, the refresh rate of most of the classic monitors is 60Hz. However, we cannot perceive the flickering of the monitor because our visual system has a lower sampling frequency. The dependence of olfactory perception on respiration posits an interesting question: if we assume that every inspiration brings in the brain a novel olfactory sample, then olfactory perception is variable in the sampling frequency. Animals take advantage of this coupling and modify their respiration according to their needs; for instance, mice at rest usually breathe at 3/4Hz, whereas during sniffing and active exploration, they reach up to around 12Hz (Wachowiak, 2011). Respiratory odor-induced changes are visible already before 200ms after the first odorized inhalation. For instance, human subjects take just up to 160ms to display differences in the nasal flowrate upon presentation of different concentrations of the same odor (Figure 4a) (Johnson et al., 2003). While for rats, differences in respiratory frequencies when comparing responses between novel and familiar odorants are already visible after 140ms (Figure 4b) (Wesson et al., 2008).

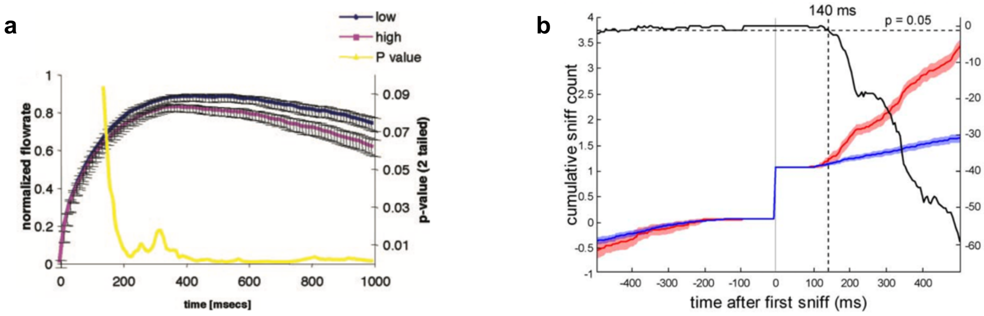

Figure 4. Odor-induced respiratory changes

(**a**) Mean intranasal flow rate for low (purple) and high (blue) concentrations of an odorant. Black trace shows the p-value of flow rate differences. Figure taken from (Johnson et al., 2003). (**b**) Differences between cumulative inhalation count over time during presentation of novel (red) and learned (blue) odorants. Black plot shows p-values for the difference between novel and learned odorants. Figure taken from (Wesson et al., 2008).

Several studies have proved how respiration is used in conjunction with head and body movements to improve olfactory sensory perception. For instance, it has been shown that mice trained to search for an odor source in a turbulent flow synchronize nose movements with sniffing during the investigation of the odor source. More precisely, specific behavioral motifs were found to correlate more with specific phases of the sniff cycle (Findley et al., 2021). Also, it has been shown that stereo olfactory cues (i.e., sensory differences between the two nostrils) can be relevant for the location of odor sources too (Catania, 2013). Coordination between head movements and respiration was also observed while rats track an odor trail on the floor; for instance, when is introduced a gap in the odor trail the rat immediately switches the search behavior, introducing wider casting sweeps to find the track again (Khan et al., 2012). The above examples, which combine sensory data collection with body movements, fall under the concept of active sensing, offering remarkable behavioral advantages as outlined above. However, the benefits of active sensing come with certain challenges, which will be discussed in the next chapter.

Movement, drawbacks of improving sensory representation

With the evolution of movement in the animal kingdom, different species could exploit new ecological niches. The advantages of movement are evident; a moving organism can interact with the environment in unprecedented ways. Movement allows animals to probe the external sensory world and collect sensory data from different perspectives, in this way building more robust internal models of what happens around them. Such an advantage, however, comes with some computational issues to solve. The movement of the sensory organ is itself a type of movement. Moving animals had to develop solutions to distinguish between reafferent inputs (i.e., inputs that come from your own movement) from exafferent inputs (i.e., inputs coming from the external world). Such general problem was solved multiple and independent times throughout evolution; every solution lays in the constraints specific for every animal (from the anatomical to the ecological domain) and the specific sensory domain.

A widespread solution is that whenever a movement is planned, a copy of the signal that is sent to initiate the movement is also sent to primary sensory structures so that those regions know that a specific movement will come soon after. This signal is referred to as efference copy and is a specific copy of the motor command sent to the effector neurons duplicated and sent to sensory neurons, too (Figure 5a). Animals, however, evolved different alternatives to solve such a widespread problem of self-movement of the sensory organs. This is generally referred to as *corollary discharge* and, even though it is still a way to deal with the same problem, can be present at different stages of the brain network and not be restricted to exact copies of the motor command (Figure 5b) (Crapse and Sommer, 2008).

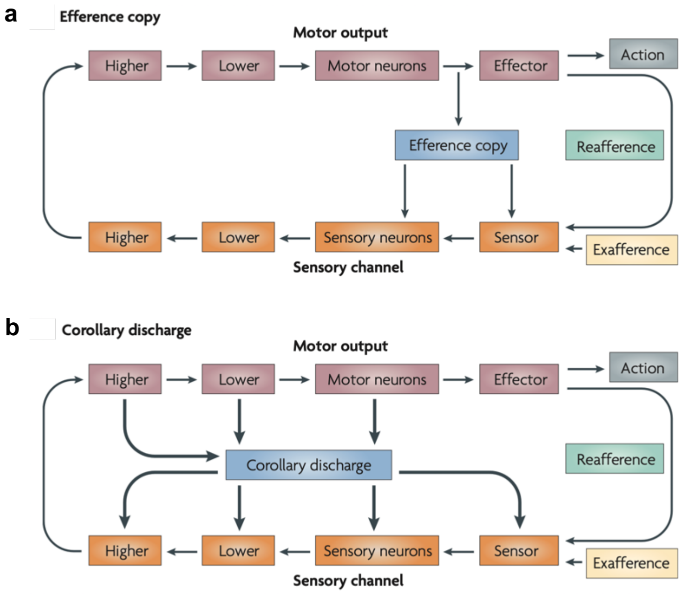

Figure 5. Efference copy versus corollary discharge

(**a**) Schematic of exafferent and reafferent inputs to the brain, the efference copy is generated at the final stage of the motor output and is sent directly to the input sensors at the sensory channel. (**b**) differently from the efference copy the corollary discharge can be seen at different stages of brain circuitry. Figure taken from (Crapse and Sommer, 2008).

To make sense of the apparent redundancy that occurs when duplicating information, one could image that different brain regions can be seen as independent observers. Every observer has only a part of the whole information collected by the brain, therefore, to disambiguate between external movements and movements of the sensory organ both information must be available to a specific observer.

In the literature, there are several examples of corollary discharge tailored to solve different problems, from reflexes to sensorimotor planning. A simple example of reflex is the avoidance response of the nematode *C. Elegans*; when the nematode encounters something that it wants to avoid, it will move forward. This forward movement starts with a reflex triggered by a stimulus at its tail. As the nematode moves forward, sensory receptors in its head detect its own motion. This detection sends signals back to the nervous system, indicating that the head is moving forward, which normally would trigger a reflex to move backward. To avoid getting stuck in a loop where the nematode keeps moving forward and then backward, special inhibitory neurons dampen the backward movement reflex so that the nematode continues its avoidance response without interruption (Crapse and Sommer, 2008).

Fish also encounter similar problems, as they produce water turbulences around them with their rhythmic movements. Fish have a special sensory system called the lateral line, which is made up of mechanosensitive hair cells that detect water movements. These hair cells are distributed along the sides of the fish’s body and head. As the fish swims, the water movement it creates activates its own lateral line hair cells. If the fish were to respond to this reafferent signal as if it were an external threat or prey, it would constantly be getting confused and might even react inappropriately, like trying to escape from its own movements. This could prevent the fish from properly detecting real external threats or stimuli, like an approaching predator or nearby prey. To avoid this confusion, when the brain sends a command to the muscles to move, it simultaneously sends an inhibitory command directly to lateral line hair cells. By doing so, it prevents the hair cells from responding to the water turbulence caused by the fish's own movement. This prevents the lateral line system from being overwhelmed by constant self-generated signals, allowing the fish to accurately detect and respond to important changes in its environment (Roberts and Russell, 1972).

Another interesting example is the weakly electric mormyrid fish, which is a well-described model for active sensing of the environment. This fish can produce electric currents from its electric organ, which are used for communication and navigation in the environment. Every time mormyrid fish generate an electric current, it also sends a copy of that current to a brain region called the electrosensory lateral line lobe; this brain region also receives direct sensory inputs from electroreceptors (Figure 6). Interestingly, reafferences coming from the electric organ to the electrosensory lateral line lobe depend on the environmental state of the animal, meaning that, for instance, they change according to the position of the fish inside a tank (Wallach and Sawtell, 2023). This allows the mormyrid fish to constantly filter self-generated electrical signals, allowing them to interpret external environmental signals accurately. A similar problem was solved inside a different medium (i.e., air) with the echolocation of bats (Crapse and Sommer, 2008).

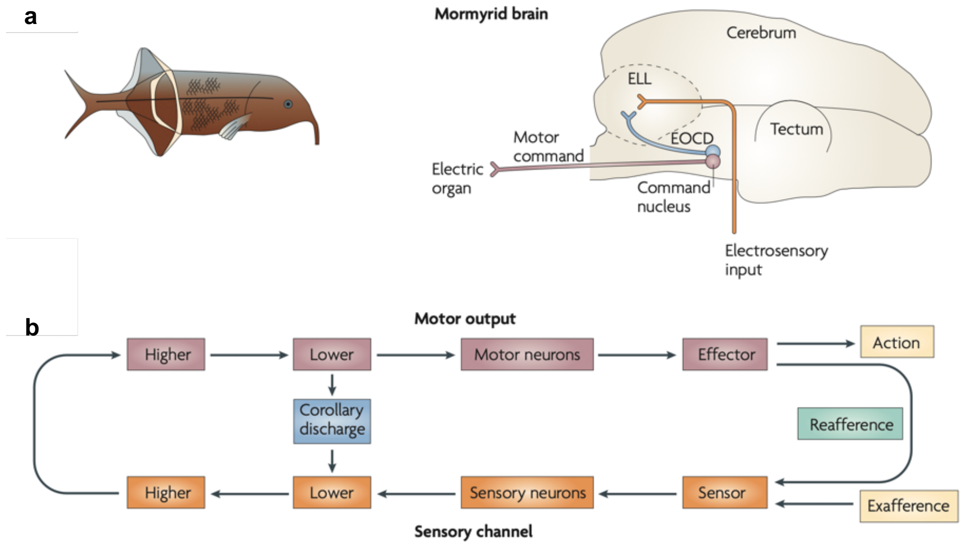

Figure 6. Corollary discharge for active sensing of the environment
(**a**) Drawings of the mormyrid fish and brain, the circuit for electro sensation is described. electric organ corollary discharge (EOCD), electrosensory lateral line lobe (ELL). (**b**) Schematic of the motor and sensory channels in the mormyrid fish brain, the blue box highlights the position in which the corollary discharge is acting in the network. Figure taken from (Crapse and Sommer, 2008).

Saccades, fast rapid eye movements, are a well-documented example of active sensing in the visual world. For instance, imagine running through a dense forest trail. Your eyes would constantly make quick movements to scan the environment; they might focus on some moving leaves on trees for an instant or on the different obstacles to find the best running trajectory on your path ahead. By doing so, saccades produce fast, homogeneous movements of the visual world on your retina; this would impinge on your ability to have a smooth perception of the visual world. Thanks to saccadic suppression, the brain filters the incoming visual information around saccades, allowing for a smoother perception. This has been demonstrated by behavioral studies in different animal models, which show that behavioral performance around saccades reaches chance levels. For instance, when a human subject looking at a screen is trained to locate a flashed square during saccade execution the performance drops rapidly when the saccade is occurring (Idrees et al., 2020) (Figure 7), suggesting a suppressive mechanism of sensory information. In the mouse model, it has been recently shown that an input from the pulvinar is sent to the primary visual cortex when a saccade occurs, ensuring uncorrelated responses of primary visual cortical neurons to external visual inputs and saccade-derived movements of the retina during the saccadic event (Miura and Scanziani, 2022).

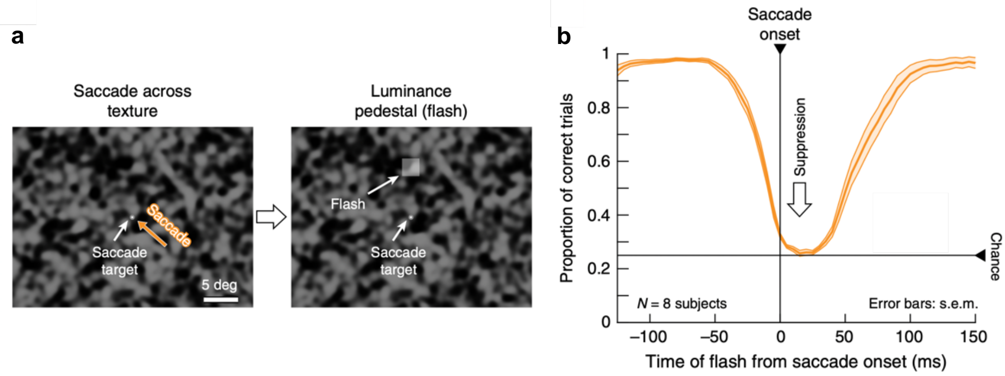

Figure 7. Chance-level behavioral performance around saccades

(**a**) Behavioral task drawing, human subjects were trained to perform saccades starting from the 4 corners towards the center. A flashed square (luminance pedestal) was then presented at 4 different locations at different temporal intervals compared to the saccade onset. (**b**) Behavioral performance expressed in terms of proportion of correct trials (y axis) as a function of saccade onset (x axis). Figure taken from (Idrees et al., 2020).

It has been also proposed that corollary discharge signals can be employed for near-future predictions in decision making tasks (Subramanian et al., 2019). If confirmed such models would suggest that corollary discharge mechanisms can be active even during the planning phases of future actions.

Sensorimotor integration in the olfactory domain is still an understudied field; indeed, motor-related control underlying the processing of olfactory information is still not well understood (Wachowiak, 2011) despite the tight link between respiration and olfaction. When looking in the brain at the known pathways that link sensorimotor integration in the olfactory domain, little is known; figure 8 shows potential pathways that can be involved. Respiratory centers in brainstem nuclei are known to control non-olfactory breathing. However, it is still not clear which pathways link the observed fast modulations of respiratory patterns upon olfactory stimulations. It has been proposed that the cerebellum and hippocampus might be good candidates for the control of the olfactomotor circuits (Mainland and Sobel, 2006). There is also evidence for an involvement of frontal cortical areas in the volitional control of breathing patterns (Tantirigama et al., 2020; Wachowiak, 2011). However, a corollary discharge-like mechanism that couples respiratory and olfactory signals is yet to be discovered.

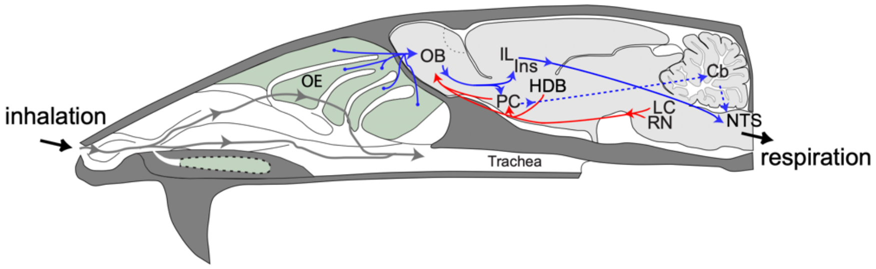

Figure 8. Sagittal section showing potential neural pathways involved in sensorimotor integration.
Gray arrows represent the passage of odor molecules. Blue arrows represent the afferent pathways while red arrows the centrifugal ones. Olfactory Epithelium (OE), Olfactory Bulb (OB), Piriform Cortex (PC), Horizontal Limb of the Diagonal Band of Broca (HDB), Infralimbic cortex (IL), Insular cortex (Ins), Locus Coeruleus (LC), Raphe Nucleus (RN), Cerebellum (Cb), Nucleus of the Solitary Tract (NTS). Figure taken from (Wachowiak, 2011).

With the advent of movement, animal evolution was funneled to develop motor systems that report their activities to sensory structures. To deal with movement-derived issues, we saw that the brain developed different elegant strategies to disentangle the source of signals. It is the coordination of sensory and motor channels that allow animals to dynamically evaluate the environment as they navigate through it.

Chemosensitivity *vs* Mechanosensitivity, an Anatomical Perspective

Chemotaxis is the movement of an organism or cell in response to a chemical stimulus. The ability to react to environmental chemicals is a universal problem in biological systems at different levels, from bacteria when searching for food and avoiding harmful environments to white blood cells when moving through the bloodstream in search of an infection site in our body to migrating cells during the development of an embryo or plant roots moving towards higher concentrations of nutrients in the soil. Some of the earliest single-celled organisms on Earth were using chemotaxis to explore and react to the environment: the story of olfactory systems, in its broadest terms, is as ancient as life. With the water-to-land transition of the first tetrapods, several drastic structural changes in the body architecture occurred simultaneously. Among those, the replacement of gills with a more efficient organ (i.e., the lung) for gas exchanges was critical, which was accompanied by the specialization of nasal cavities to filter, warm, and humidify the incoming air. The olfactory system evolved together with respiration, employing the nasal cavities as an efficient site for olfactory reception; this brought to the evolution of the olfactory epithelium, a specialized site for the detection of odor molecules which developed on top of the convoluted turbinate bones, for an increased surface and efficiency. As described before, respiration is used to actively sample the olfactory environment and is efficiently used in different behavioral strategies to improve sensory perception. Respiration can be seen as a specialized form of movement, allowing to bring an air sample proximal to the nostrils ready to be perceived. It is reasonable to suppose that the increased efficiency of air sampling was the reason why olfaction specialized inside the nasal cavities of terrestrial vertebrates. In line with the above assumption, it was found that mammalian olfactory sensory neurons (OSNs) can act not only as odor detectors but also as mechanical sensors in response to airflow stimulation (Grosmaitre et al., 2007).

The seminal study of Grosmaitre et al., 2007 showed that both the septal organ and main olfactory epithelial sensory neurons are mechanosensitive. This was demonstrated by performing patch-clamp recording on OSNs in *ex-vivo* preparations of the olfactory epithelium. Recorded cells were stimulated with protocols of different puffing pressures and distances to induce mechanical stimulation both with odors and without, and OSNs showed a tuning for puffing pressure, which was also dependent on the distance. However, it is important to note that such results have not yet been replicated. As described before, the field potential in the olfactory bulb shows a strong coherence with the respiratory activity (Figure 9a). Vertebrate chemosensation is mediated via G-protein coupled receptors (GPCRs) of different types; once the odor molecule binds to the receptor, it initiates an intracellular cascade through the cAMP pathway that enables the consequent opening of the cyclic nucleotide-gated (CNG) channels which in turn depolarize olfactory sensory neurons and trigger action potentials (Kaupp, 2010). Grosmaitre et al., 2007 showed that by knocking out the cyclic nucleotide-gated channel *Cnga2,* the observed coherence between respiration and field potential in the olfactory bulb of anesthetized mice disappeared (Figure 9b). Also, OSNs *Cnga2*$^{-/y}$ knockout mice were unresponsive to both odorants and mechanical stimuli in *ex-vivo* preparations.

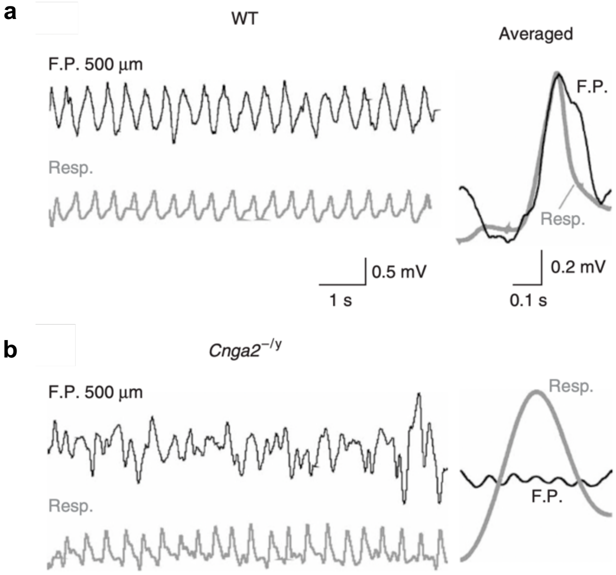

Figure 9. Uncoupling of respiration and filed potential in the olfactory bulb.

(**a**) Recording of anesthetized mouse at 500μm depth in the olfactory bulb, on the left are shown examples traces of both respiration and field potential (F.P.), on the right is the averaged field potential aligned to the respiration (**b**) Same as the up figure but for *Cnga2*$^{-/y}$ knockout mouse, the absence of coherence between respiration and field potential can be observed on the right. Figure take from (Grosmaitre et al., 2007).

The same group later characterized more in detail the different types of odorant receptors expressed by OSNs; depending on their expression, the mechanosensitivity of OSNs varied. Thanks to gain and loss-of-function experiments, they demonstrated that odorant receptors are necessary and sufficient for the mechanosensitivity of OSNs (Connelly et al., 2015). However, these results were only demonstrated in *ex-vivo* and *in-vitro* preparations, and a better *in-vivo* characterization of the mechanosensitive role of different odorant receptors at the physiological and behavioral levels is needed. Overall, there is strong evidence that at least some mammalian OSNs are not only sensitive to odor molecules but also to mechanical stimulation. OSN mechanosensitivity can be seen as one of the signatures of the tight bond between respiration and olfactory sensation in vertebrates, but as described before, it is not the only one. Respiratory-coupled oscillations were described in olfactory regions and olfactory processing follows the constrains imposed by breathing and developed its physiological activity around it. For instance, mitral/tufted cells in the olfactory bulb show precise sniff-locked activity and tile the duration of the sniff cycle, representing all phases of respiratory events (Shusterman et al., 2011). Moreover, active modulation of respiration through sniffing was shown to modulate the responsiveness of mitral/tufted cells, enhancing odor representation (Jordan et al., 2018a).

It is very interesting to compare the different strategies that animals adopted to solve similar problems in the fight for representation of the sensory world, considering the species-specific anatomical constraints that every animal has. An interesting example is one of the arthropods; they “breathe” through a tracheal system composed of spiracles, small openings on the sides of their bodies, connected through a system of tubes called tracheae that arborize inside the insect body to oxygenate tissues. Arthropod’s olfactory system instead develops on antennae located on the head of the insect, which is equipped with sensory receptors called olfactory sensilla, specialized to detect odors in the environment (Kaupp, 2010). Arthropods thus show independent olfactory and respiratory systems. For instance, when tracking an odor plume, differently from mice that use active sniffing coupled with head movements to search for the target location (Findley et al., 2021) it has been shown that locusts actively move their antennae to search for odorant location. This active search strategy, like sniffing in mice, has an impact on the frequency of the sampled odor, improving information about odor location (Huston et al., 2015).

Differently from mammals, it is not known whether arthropods show mechanosensitivity in olfactory receptors; however, it is known that their olfaction relies on receptors that are both structurally and genetically unrelated to the vertebrate receptors (Kaupp, 2010). A deeply studied arthropod is *Drosophila*, where a fascinating model has been formulated to describe its olfactory navigation circuit (Figure 10) (Steele et al., 2023). This model takes into consideration three main actors: (I) the odor information, coming from the olfactory pathway and innervating the fan-shaped body (FB) through tangential inputs (FBt neurons), (II) the heading signal, carried by compass neurons (EPGs) in the ellipsoid body (EB) to the fan-shaped body through a protocerebral bridge (PB). (**III**) the external airflow information, carried by PFN neurons to the fan-shaped body from the noduli (NO). The same PFN neurons also carry the information of the heading through the PB. Thanks to this anatomical arrangement, they identified a class of neurons ($h\Delta C$) in the fan-shaped body able to integrate these two independent channels of information showing odor-gated wind-direction tuned signals (Steele et al., 2023).

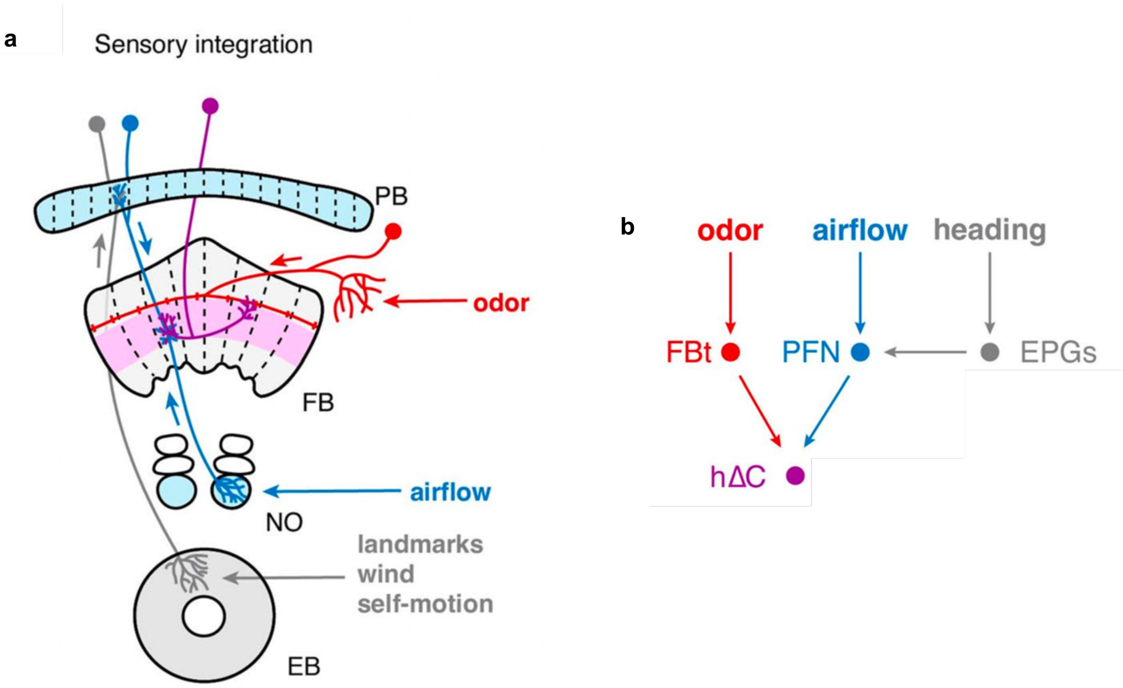

Figure 10. An olfactory navigation circuit in Drosophila
(**a**) Anatomical drawing of the navigation circuit. protocerebral bridge (PB), fan-shaped body (FB), noduli (NO), ellipsoid body (EB) (**b**) Schematic of the model showing neuron's names color coded in the left drawing. Figure taken from (Steele et al., 2023).

It is interesting to note that in Drosophila the olfactory and mechanosensory (external airflow and heading) channels are independent at the acquisition stage at the sensory periphery and are integrated at a later stage. In vertebrates, the parallel acquisition of olfactory and mechanosensory signals from the same olfactory receptors in the olfactory epithelium poses a problem: how can a change in concentration be distinguished from a change in airflow speed if the two channels are acquired from the same sensor? This problem will be addressed in depth in the next chapter.

The Challenge of Representing Odor Concentration

Let's imagine that a sensor must identify the concentration of an odor; the sensor works in a way that, by active suction of air, detects molecules; the higher the number of molecules in the sampled air, the higher the sensor's response. Unfortunately, the sensor is not working very well, and it unpredictably switches between a low and a fast suction state. The suction state has an impact on the amount of sampled air in the same unit of time, thus affecting the sensor's signal. In this example, how could an external observer, by looking at the sensor's output, distinguish an increase in odor molecules from a low-to-fast switch in the suction state? We would need to have another sensor to track the profile of the suction states to correctly infer the odor concentration.

The fact that olfactory sensory neurons can act both as olfactory and mechanical sensors could be a good solution to the problem described in the above example. However, these two sensory streams look to be embedded in the same olfactory receptor, making apparently impossible to disentangle the two information. This is also mirrored in the activity of neurons in the olfactory bulb: Figure 11 shows the response of two example neurons in three different conditions when comparing an increase in odor concentration (green condition) with an increase in inhalation speed (pink condition), the change in firing rates was very similar (Jordan et al., 2018b). Even response latencies were extremely comparable in the above two conditions, meaning that a faster inhalation shifted responses in the olfactory bulb comparably to an increase in odor concentration (Jordan et al., 2018b).

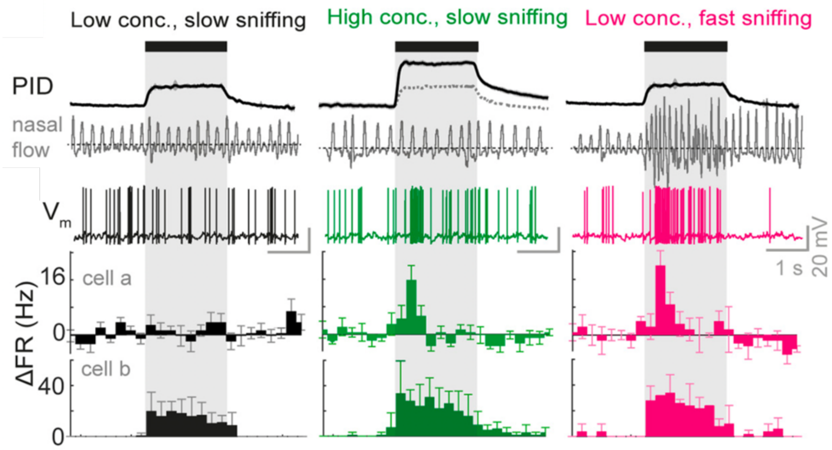

Figure 11. Whole cell recordings of Mitral/Tufted cells.

The above plot show photoionizing detector (PID) traces of odor concentration together with the nasal flow of the mouse. Below are show two peristimulus time histograms (cell a, cell b) together with the raw response trace of cell a. Figure taken from (Jordan et al., 2018b).

By looking at the activity of the recorded mitral/tufted cells in Figure 11, a downstream observer (like the piriform cortex) would not be able to tell apart the two conditions. However, behavioral experiments point in a different direction. Jordan et al., 2018b trained mice in a head-fixed go/no-go task to distinguish five concentrations of the same odor to get a reward. Half of the mice were trained in a high-go condition, while the other half were in a low-go condition.

When splitting behavioral performance between fast and slow sniffs, they observed that the concentration discrimination performance was not influenced by the variance introduced by the inhalation speed (Figure 12a, b). More precisely, there was a tendency for higher go rates in both high-go and low-go conditions. However, this tendency was not different across the different concentrations, making it more likely to explain this tendency with the fact that there is a correlation between faster sniffing and higher motivation to perform the task (Jordan et al., 2018a).

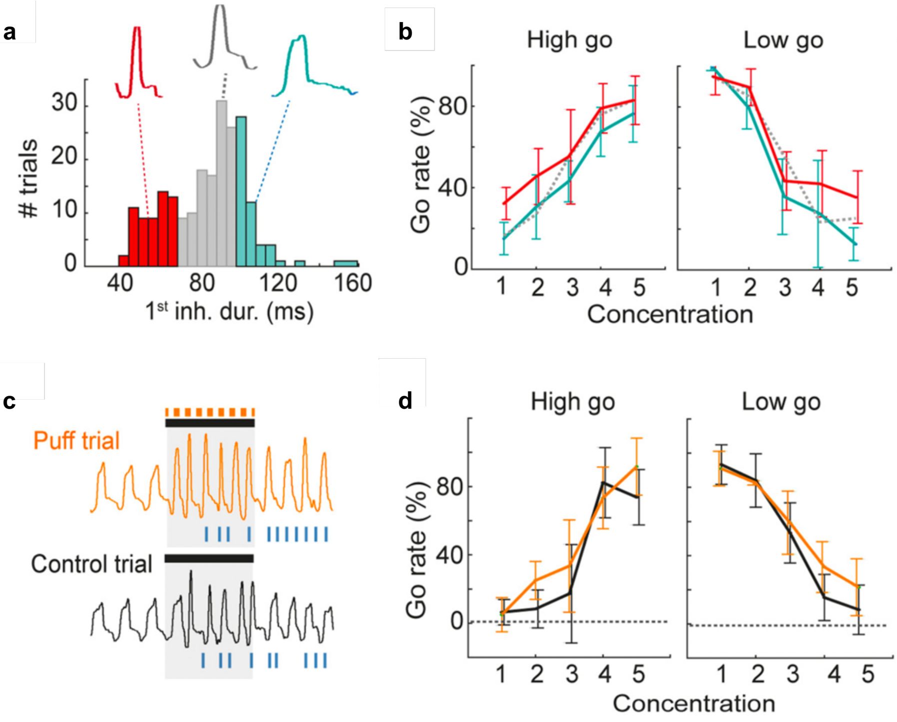

Figure 12. Behavioral performance is not affected by inhalation variability

(**a**) Distribution of the first inhalations upon odor presentation color-coded for the fast (red) and slow (cyan) fractions used in the right plot. Gray is the full distribution; (**b**) Mice performance level indicated as go rate (%) both for high-go condition (go concentrations are 4 and 5) and for the low-go condition (go concentrations are 1 and 2); (**c**) Two examples of respiratory traces during control trials and air-puff trials, blue ticks indicate licking times. (**d**) Same plot as in b, this time however control trials (black) are compared with puff trials (orange). Figure taken from (Jordan et al., 2018b).

Moreover, when externally modifying inhalation speed by applying an air puff to the flank of the mouse (which induces a reflex sniff reaction) again, the performance in discriminating subtle changes in odor concentration was not affected (Figure 12c, d), further confirming that sniffing variability (i.e., the airflow velocity inside the nasal cavities) is not a confounding effect but rather a feature of olfactory behavior. Similar behavioral results were also described in humans: subjects were trained to perform strong and weak inhalations by matching two respiratory patterns in an oscilloscope. During the experiment, they had to perform either strong or weak inhalations and report the odor concentration that they smelled. Results showed that subjects were able to tell apart odor concentration independently of the sniffing vigor (Teghtsoonian and Teghtsoonian, 1978).

How do we reconcile behavioral data with physiology? A proposed solution is that the olfactory bulb represents how fast an animal is breathing. Indeed, the same paper (Jordan et al., 2018b) shows that a simple linear model is able to predict the inhalation duration by feeding it with the peak spike rate of the recorded cells during different types of respiratory events. Coherently, it has been shown that response latency (more prominently in mitral cells) depends on sniffing velocity (Mainland et al., 2014). This suggests that the olfactory bulb holds all the information necessary to discriminate a change in concentration from a change in inhalation speed employing a temporal code strategy. It has also been shown that a fluid dynamic model that considers odor dynamics in the nasal cavities is able to best represent odor concentration invariantly to sniffing velocity (Shusterman et al., 2018). An alternative spatial model comes from the observation that the response latency between lateral to medial mitral/tufted cells is different according to odor concentration. This means that low odor concentrations result in a high lag between lateral and medial observed responses, while at increasing concentrations, this lag shortens (Zhou and Belluscio, 2012). However, this model was drawn on data obtained from anesthetized mice, thus not taking in consideration the variability introduced by sniffing. For this model to work in awake states, there must be a further separation at the level of the epithelium; for example, slow inhalations activate only part of the olfactory epithelium, and with faster inhalations, odor molecules reach other regions of the epithelium. Given the observed responses in mitral/tufted cells of Jordan et al., 2018b (Figure 11) it is still unclear whether the olfactory bulb can extract a sniff invariant representation of odor concentration.

The transformation that occurs when going from the topographic representation in the olfactory bulb to distributed one in the piriform cortex changes the logic with which neurons process information (Figure 13). The piriform cortex represents odor information through a distributed and sparsified code (Fulton et al., 2024; Stettler and Axel, 2009). Such representation is not hard-coded but can change with time and experience (Pashkovski et al., 2020; Schoonover et al., 2021).

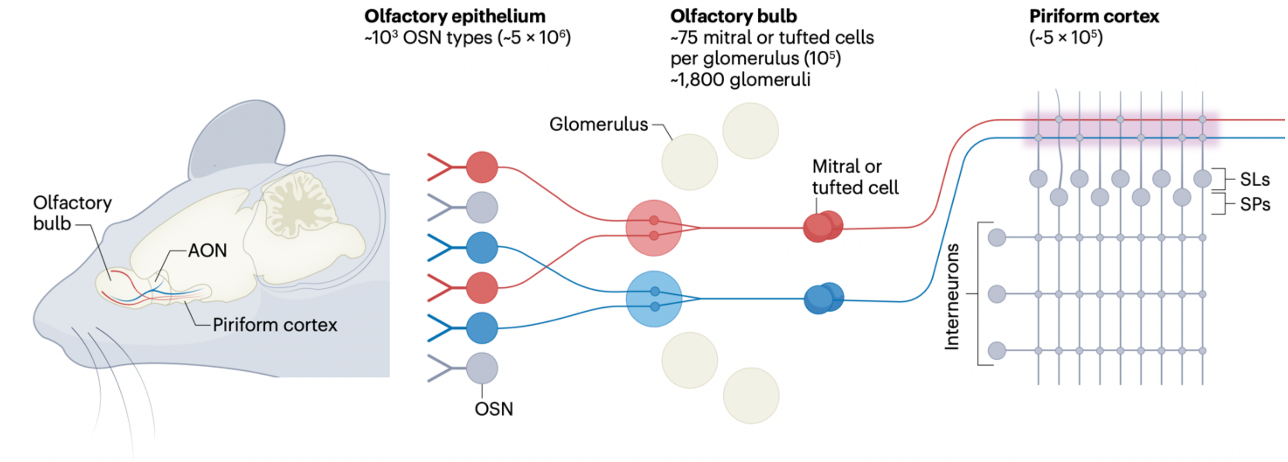

Figure 13. Basic anatomy of the olfactory system

Every Olfactory Sensory Neuron (OSN) in the olfactory epithelium express a specific olfactory receptor (OR). Information from OSNs reaches the olfactory bulbs in an organized and topographic manner. Mitral and Tufted cells, the output neurons of the olfactory bulb, send projections mainly to the piriform cortex, the latter lacks a topographic representation of odor information but rather works tanks to distributed activity of the neural population. Semilunar cells (SLs), superficial pyramidal cells (SPs). Figure taken from (Fulton et al., 2024).

When talking about odor concentration representation in the piriform cortex two important aspects of the same phenomenon must be discussed. On one side, there is the importance of classifying an odor independently from its concentration (e.g., I always want to recognize the scent of smoke indicating a fire, no matter how faint); on the other side, it is also relevant to represent its concentration/intensity (e.g., for instance when trying to localize the source of the smoke). These problems require different coding strategies, which might coexist in the piriform cortex and be summoned depending on the behavioral goals. The ‘primacy coding’ model (Wilson et al., 2017) suggests that early responses during an inhalation correspond to the responses of OSNs with the highest affinity for the sampled odor molecules. By decoding odor identity during these early moments of every sampling event (i.e., inspiration) the olfactory cortex would be able to represent the most relevant molecules in that inspiratory sample, potentially producing a concentration-invariant representation of odors. Recently, it was shown that thanks to the anatomical circuitry of the piriform cortex (i.e., recurrent feedback inhibitory activity), the early inputs of an inhalation coming from the olfactory bulb activate pyramidal cells in the piriform cortex. The first pyramidal cells that are active (the ones that receive the strongest inputs by mitral/tufted cells for the specific odor) immediately recruit feedback inhibition that suppresses the surrounding cells (Bolding and Franks, 2018). This mechanism would allow the cortex to maintain a stable representation across odor concentrations. Odor intensity, instead, is thought to be encoded by a parallel population of cortical neurons that is tuned to odor concentration by changing its response latency and employing temporal features of the stimulus (Bolding and Franks, 2017).

The absence of topographic representations of both odors and respiratory activity in the piriform cortex makes the piriform cortex a suitable region to employ a population code to solve biological problems. This anatomical arrangement is inherently different when compared to retinotopic maps in the cortex, in the superior colliculus or to the barrel cortex representing whiskers. However, going beyond the anatomical topography, orthogonal representation of different behaviors is found throughout the cortex and happens to be a canonical strategy to represent behavioral dimensions that co-occur in time but must not collide to work properly (Stringer et al., 2019). This can be explained by the fact that cells in the brain both cooperate and perform parallel independent computations ensuring that different neural representations can coexist and function effectively without clashing.

RESULTS

The influence of Breathing on Odor-Related Neural Activity in the Piriform Cortex

To study how perceptual stability in the olfactory domain might be altered by respiratory sampling, I focused my experiments on awake head-fixed mice. Such an approach allowed me to record the breathing activity of the mouse with a fine-temporal resolution, highlighting respiratory features that, at a later stage, were critical to classifying respiratory events. Also, I could precisely present and control several odor stimuli at different concentrations while acutely recording the activity of about a hundred single units in the anterior piriform cortex of most of the recorded mice (Figure 14). Since my scientific questions were pointing to the neurophysiology of sensory stability, the selection of the odors used was thought to avoid any known natural valence for mice, favoring instead neutral stimuli, to avoid strong innate behavioral responses. Odors (*alpha-pinene, eucalyptol, limonene, methyl butyrate, eugenol, dicyclohexyl disulfide, methyl 2-furoate, p-cymene*) were also selected based on their visualization at the photoionizing detector (PID), favoring odors that showed faster rise time and a stable trace.

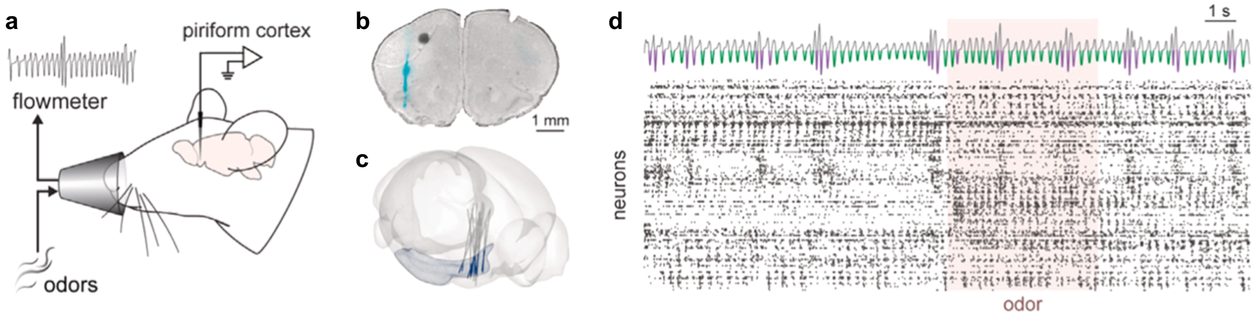

Figure 14. Experimental setup along with an example of processed data

(**a**) Schematic drawing showing the experimental setup. (**b**) Coronal section showing a recording site (cyan) at the level of the anterior piriform cortex. (**c**) Reconstruction of recording sites from all experiments (n = 22 mice), blue mask shows the limits of the piriform cortex. (**d**) Example raster plot showing a recorded population of neurons along with the respiratory trace of the mouse, inspiratory events are color coded as slow (green) and fast (purple) inhalations, see the text below for the classification pipeline. Shaded area is the odor period (5 s).

By looking at the neural activity patterns in Figure 14, it is evident that a considerable fraction of recorded neurons in the piriform cortex show a repetitive activity that has some correlation with respiration.

Indeed, a Support Vector Regression (SVR) decoder was remarkably good in predicting the phase of the inhalation by training it with a low-dimensional embedding of the neural population activity (Figure 15a, b) (see methods section: Concentration decoding). Such results were then graphically confirmed by plotting the first two principal components of the neural population trajectories color-coded with the phase of inhalations (Figure 15c). Overall, this beautifully shows that even a population of just over a hundred neurons in the piriform cortex contains the information necessary to track the phase of every respiratory cycle.

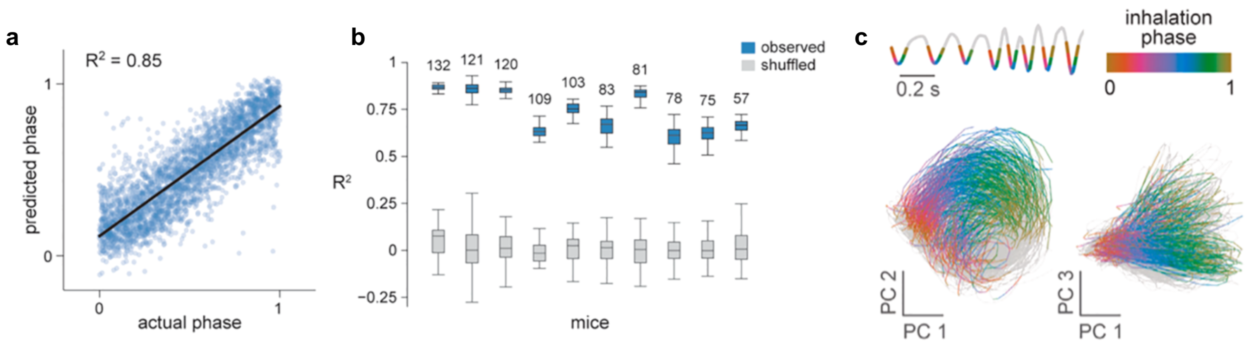

Figure 15. Inhalation phase decoding

(**a**) Scatter plot showing the actual and predicted inhalation phase for an example mouse (n = 120 neurons), every point in the plot is the neural population PCA embedding in a time bin of 10ms for every phase of the inhalation. The actual inhalation phase was spanned from 0 (inhalation onset) to 1 (inhalation offset). (**b**) Plot showing on the Y axes the goodness of prediction (R^2) using the neural trajectories for every mouse (blue). In grey is shown the null distribution, built by randomizing the inhalation phase before the prediction. The number of neurons for every mouse is indicated above each boxplot. (**c**) Plots showing the first three principal components of neural population trajectories during individual respiratory cycles of an example mouse. Only inhalation phase is color-coded while the exhalation is grey.

From a behavioral perspective, by observing the respiratory trace (see Figure 14d), even in the absence of odor stimuli, mice alternated slow inhalations (at ~4Hz) with small bouts of faster inhalations (that could reach up to ~15Hz) at variable frequencies. Inhalation events were thus classified as slow or fast inhalations based on the features of the inhalation waveforms (Figure 16). Briefly, a matrix of 100ms chunks of the respiratory trace centered on the inspiration peak was input to the pipeline for the following classification. As the first step, Principal Component Analysis (PCA) was applied to reduce the dimensionality of the input matrix. Secondly, the N-dimensional subspace that explained 98% of the variance was used as input to a Gaussian Mixture Model for the clustering. Lastly, the average waveforms of each output cluster were then further classified with a hierarchical clustering algorithm to finally output the two more different inhalation clusters, which were finally assigned as slow (green) and fast (purple) inhalation clusters based on their average inhalation length (see methods section: Inhalation clustering).

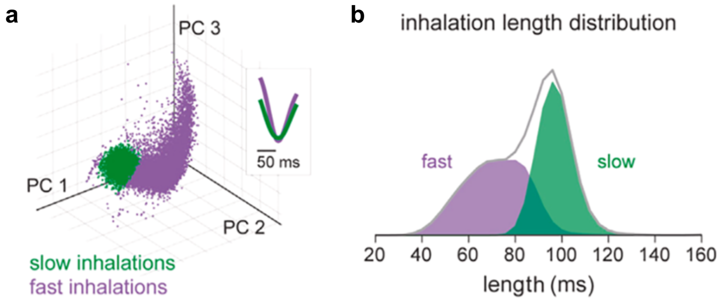

Figure 16. Features and length distribution of the inhalation types

(**a**) Plot showing the first three principal components of the inhalation waveforms color coded after performing a Gaussian-mixture model hierarchical clustering. The inset shows the average waveform for both slow and fast inhalations. (**b**) Distributions of fast and slow inhalations after the classification, the full distribution is shown in grey.

Such classification of inspiratory events was fundamental for the subsequent analyses. It revealed that the neural population trajectories not only faithfully tracked the phase of each inhalation but also the speed. Indeed, when trying to decode the inhalation speed with a linear Support Vector Machine (lSVM) classifier, feeding it with the mean firing rate calculated over a 180ms window starting from the inhalation onset, it was able to reliably classify fast versus slow inhalations (previously classified with the inspiration clustering pipeline) (Figure 17a). When plotting the neural population trajectories for the same example mouse from Figure 15, color-coding the inspiratory types (fast, slow) clearly shows that the information speed lies on the third principal component (Figure 17b).

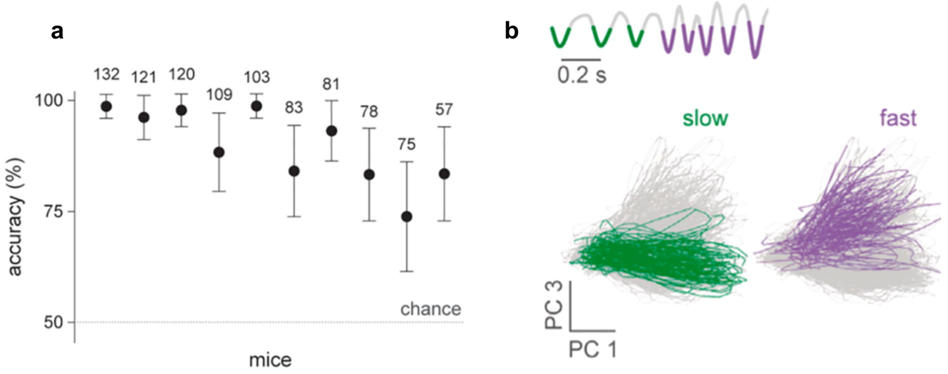

Figure 17. Inhalation speed decoding
(**a**) inhalation speed decoding (fast versus slow) for every individual mouse using a lSVM, the number of neurons for every mouse is shown above each dot, chance level is at 50% accuracy. (**b**) Same neural trajectories as in Figure 15c, color coded according to the inhalation speed. Green, slow inhalations; purple, fast inhalations.

Digging more into the data, I started to analyze single-unit responses to changes during different inhalation speeds, focusing on the odor presentation window. Odor stimuli lasted 5 seconds, which allowed for a good distribution of the different inhalation speeds sampled by the mouse during stimulus presentation (see Figure 14d). The following analyses focused on the fraction of single units responsive to at least one odor concentration (205 of 660 neurons, n = 6 mice).

After splitting fast and slow inhalations classified before and by looking at the average firing rate of every unit in the first 180ms window from the inhalation onset, it was striking to observe that more than 70% of odor-responsive neurons were changing their responses according to the inhalation type during the odor presentation window. The effect of inhalation speed on the average firing rate of neurons was diverse, with a fraction of neurons increasing their firing while others decreasing it (Figure 18). Of the 750 odor-concentration response pairs obtained from the odor-responsive neurons, almost 60% were affected by the inhalation speed (Figure 18c).

To give a quantitative intuition of the effects of these changes Figure 19 compares, for every neuron-odor pair, the change that was produced by a slow-to-fast inhalation switch and a 10-fold increase in odor concentration. Remarkably, the response change in neurons caused by a change in the inhalation speed was not only comparable but, in terms of distribution, even higher than the one caused by a change in odor concentration. Such observation suggests that the variability that is introduced during every inhalation can be a considerable challenge for the discriminability of odor concentrations.

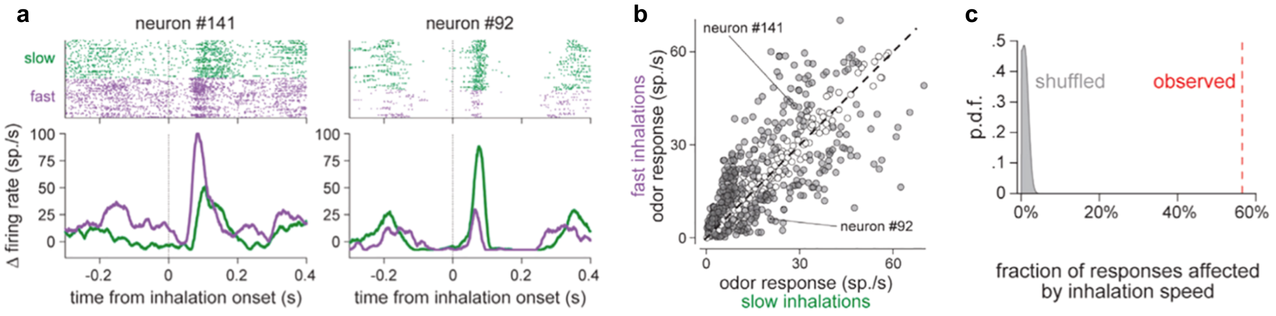

Figure 18. Odor responses during slow and fast inhalations

(**a**) Raster plot and Peri Event Time Histogram (PETH) of two example neurons from the same mouse, zero is the inhalation onset. (**b**) scatterplot of odor-responses (five odors, 0.01% and 0.1% v/v concentration; n = 750 odor-concentration responses) for all odor-responsive neurons (Benjamini-Hochberg adjusted $p < 0.05$, Wilcoxon signed-rank test; n = 205 neurons, 6 mice). Gray dots, significant difference between the amplitudes of the responses during fast and slow inhalations. White dots, no statistical difference ($p < 0.01$, two-sided Wilcoxon rank-sum test). Responses of neurons in the left panel are indicated. (**c**) Fraction of concentration responses changing with inhalation speed (red vertical line) and null distribution obtained by shuffling 1,000 times the inhalation speed label for each concentration response.

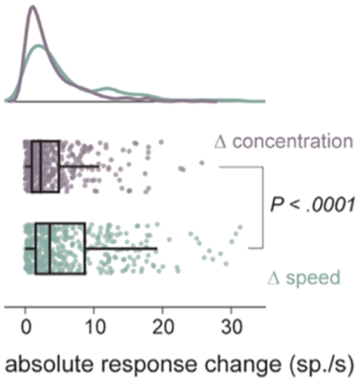

Figure 19. Comparison of a change in concentration and a change in inhalation speed

Absolute change in firing rate due to a 0.01%-to-0.1% change in odor concentration and a slow-to-fast switch in inhalation of the 0.01% odor (n = 477 neuron-odor pairs; $p < 0.0001$, Wilcoxon signed-rank test). Probability density function (top) along with boxplots (bottom) are shown.

To provide a qualitative understanding of the potential problem that is generated with variable inspiratory sampling, figure 20a shows the activity of an example neuron; such neuron shows an increase in the firing rate both when there is an odor concentration increase and with a faster inhalation. The increase in firing of this neuron after the inhalation onset is equivalent for both stimuli, raising the issue (just by reading the firing rate of this single neuron) of not knowing whether there was an increase in external odor concentration or an increase in inhalation speed. This is not a phenomenon that is limited to the example neuron shown here. To better quantify this, figure 20b calculates a concentration-discrimination index (CDI) for every odor-responsive neuron. The CDI was computed using the spike counts during the inhalation at two different odor concentrations and by performing its area-under-the-receiver-operating-curve (auROC) (see methods section: Concentration discrimination index). When calculating the CDI across different inhalation speeds the discrimination index decreases, supporting the idea that the variability in the inhalation speed have an impact on concentration discriminability.

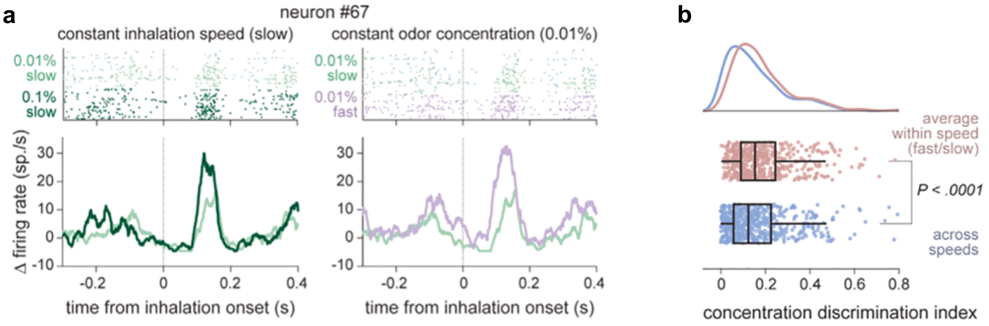

Figure 20. Example responses for different odor concentration and inhalation speed along with Concentration discrimination index

(**a**) Raster plot and Peri Event Time Histogram (PETH) of an example neuron to different concentration and inhalation speeds, zero is the inhalation onset. (**b**) Concentration discrimination index (CDI) calculated for all odor-responsive neurons, the plot shows the difference between the CDI calculated within and across inhalation speeds ($p < 0.0001$, Wilcoxon signed-rank test) for two different odor concentrations (0.01 and 0.1% v./v. odorant).

Together, these results show the strong impact of respiratory activity in the primary olfactory cortex. Such effects are widespread among odor-responsive neurons and might have a considerable impact in the discrimination of odor concentration at the single neuron level, posing a problem when trying to extract the external odor concentration at every inspiratory sampling.

Heterogenous Neural Responses to Olfactory and Non-Olfactory Inputs

By observing the behavior of neurons in the piriform cortex in response to different odor concentrations and inhalation speed, it was clear that the observed responses were not solely due to olfactory inputs. Indeed, some neurons showed opposite tuning for odor concentration and inhalation speed (Figure 21). If the responses were purely due to olfactory inputs, the changes in amplitude would be consistently tied to odor concentration only. However, the observed variability with inhalation speed suggests another factor is at play. Non-olfactory input might include sensory feedback related to the mechanics of breathing, such as signals from the respiratory system, which are independent of the odorant itself. Alternatively, sniffing at different speeds can change how odorants are deposited onto the olfactory epithelium. Faster inhalations might cause a different pattern of airflow and odorant contact inside the nasal cavities, which can alter the neural response.

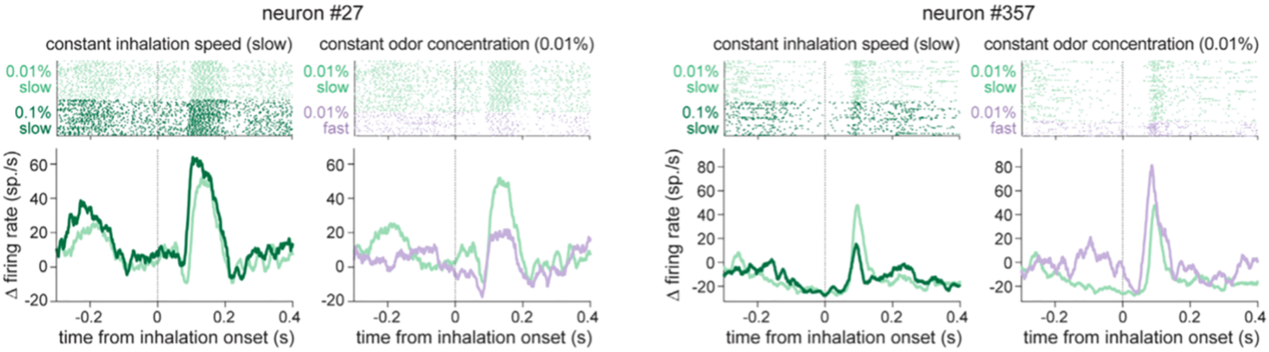

Figure 21. Examples of neural responses

Raster plot and Peri Event Time Histogram (PETH) of two example neurons showing different behaviors to increase concentration and inhalation speed.

To quantify the relationship between the odorant concentration encoding and this non-olfactory input, a generalized linear model (GLM) was fit to the responses of neurons in the piriform cortex to the different stimuli (odor concentrations and inhalation speeds). Specifically, the GLM had three factors: odor concentration (0%, 0.01%, 0.1%, and 1% v/v), inhalation speed (slow or fast), and the interaction between inhalation speed and concentration (Figure 22a) (see methods section: Encoding models). The GLM model aimed to predict the spike count of neurons in a 180ms window aligned to inhalation onset during every inhalation event. The model explained 91.9% of the variance in the mean number of spikes generated by every neuron during the selected window.

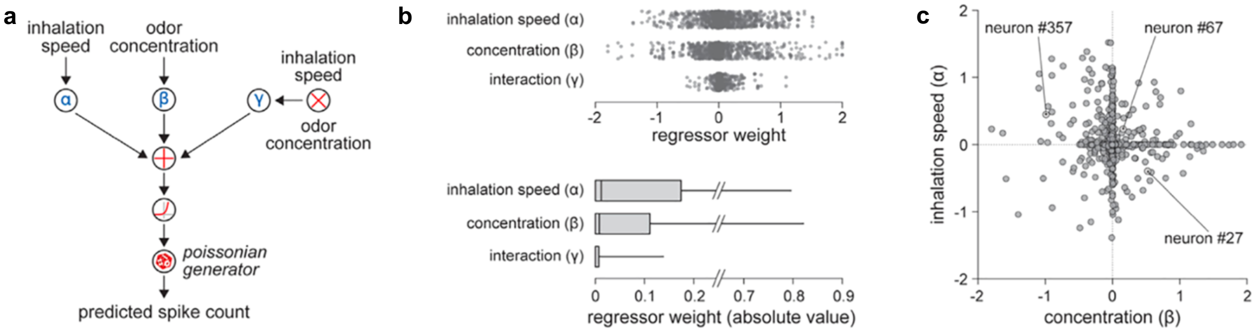

Figure 22. Generalized Linear Model (GLM) model

(**a**) Schematic drawing of the GLM model. (**b**) On top is shown distribution of the regularized regressor weights for inhalation speed, odor concentration, and their interaction (n = 928 neuron-odor pairs; 2 odors; 4 mice). On bottom is shown the boxplot of the absolute values of the regularized regressor weights. (**c**) Scatterplot of the concentration and inhalation speed regressor weights. Each data point is a neuron-odor pair (n = 928 neuron-odor pairs; 2 odors; 4 mice). Neurons #27 and #357 of figure 21 and neuron #67 of figure 20 are indicated.

The combined effect of inhalation speed and odor concentration (i.e., the interaction term γ) on the odor response amplitude is minimal (Figure 22b). This means that the impact of changing inhalation speed and odor concentration together does not significantly alter the response amplitude beyond their individual effects. In other words, this suggests that the combined influence of these two factors on odor response amplitude is minimal. Implying that inhalation speed and odor concentration primarily affect odor responses independently, with the main effects of each variable being the primary drivers of the neural response.

More importantly, the population of neurons in the piriform cortex showed heterogeneous responses to the combination of olfactory and non-olfactory sensitivities, producing a homogenous representation of the inhalation speed and concentration factors (Figure 22c). When the same analysis was restricted to the early 70ms window, similar results were produced after the inhalation onset (Figure 23a, b, c). When classifying regular spiking (RS) and fast-spiking (FS) neurons (see methods section: Spike sorting and inclusion criteria), similar results were found, suggesting that the distribution of non-olfactory and olfactory sensitivities was heterogeneous across these two subpopulations of neurons (Figure 23d, e).

Overall, the GLM model shows that the variability in odor responses with different inhalation speeds is not primarily due to how the speed interacts with odor concentration. Instead, inhalation speed itself, as a separate factor, affects the response amplitude. This means that the neural responses are not solely due to odor concentration but are also affected by the mechanics of sniffing. The integration of both olfactory and non-olfactory inputs results in complex response patterns, indicating that the piriform cortex processes a combination of sensory information from both the odorant and the act of inhalation.

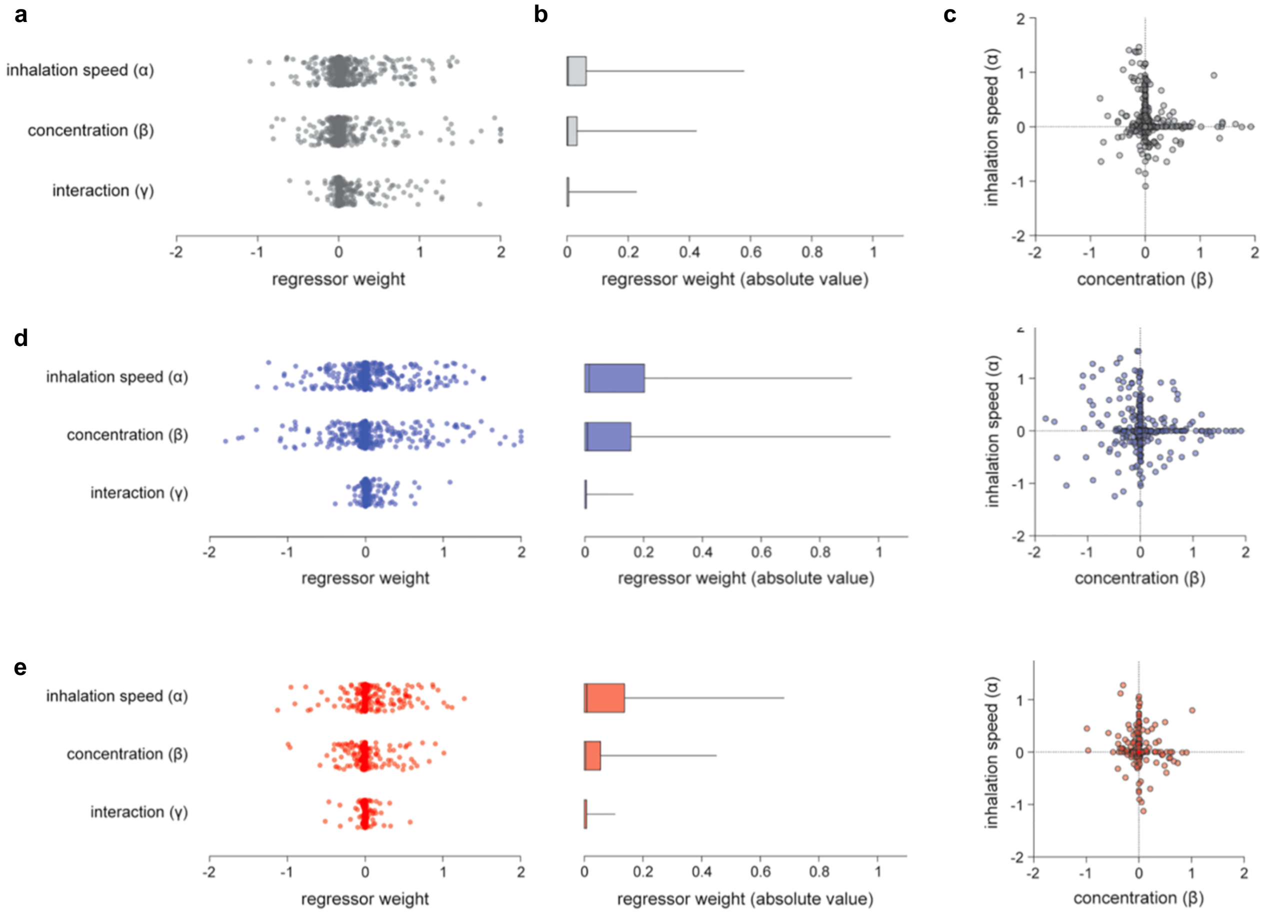

Figure 23. Generalized Linear Model (GLM) model using 70ms window and after cell-type clustering

(**a**) Distribution of the regularized regressor weights for inhalation speed, odor concentration, and their interaction using a 70ms window (n = 928 neuron-odor pairs; 2 odors; 4 mice). (**b**) Boxplot of the absolute values of the regularized regressor weights shown in (a). (**c**) Scatterplot of the concentration and inhalation speed regressor weights shown in (a). Each data point is a neuron-odor pair (n = 928 neuron-odor pairs; 2 odors; 4 mice). (**d**) same as the above a, b, c plots but for regular spiking (RS) subpopulation in blue (578 neuron-odor pairs), here a 180ms window was used. (**e**) same as the above a, b, c plots but for fast spiking (FS) subpopulation in red (350 neuron-odor pairs), here a 180ms window was used.

Nasal Airflow Rate is Signaled to the Piriform Cortex via Mechanosensation

The non-olfactory input that independently modulates the activity in the piriform cortex might either originate directly from the airflow passage in the nasal cavities or from a signal generated from respiratory centers located in the brainstem (for instance, the preBötzinger complex (Del Negro et al., 2018)). Given the absence of a known direct connection between such brainstem centers and the piriform cortex in literature, the more parsimonious option was first explored. Indeed, it was also shown in humans that both the act of sniffing and the passive blowing of non-odorized air in the nasal cavities entrain the piriform cortex (Sobel et al., 1998). To experimentally manipulate the airflow passage through the nostrils, a tracheostomy was performed in anesthetized mice (see methods section: Surgical procedures for *in Vivo* extracellular recordings). This procedure excluded the nasal cavities from the pulmonary system, still allowing the anesthetized mouse to breathe autonomously (Figure 24a). When looking at the baseline activity of piriform cortical neurons, the normal respiratory entrainment seen in control mice (see Figure 21 for examples) was lost; this was quantified in Figure 24b by showing the average activity of the recorded neurons aligned to the inhalation onset.

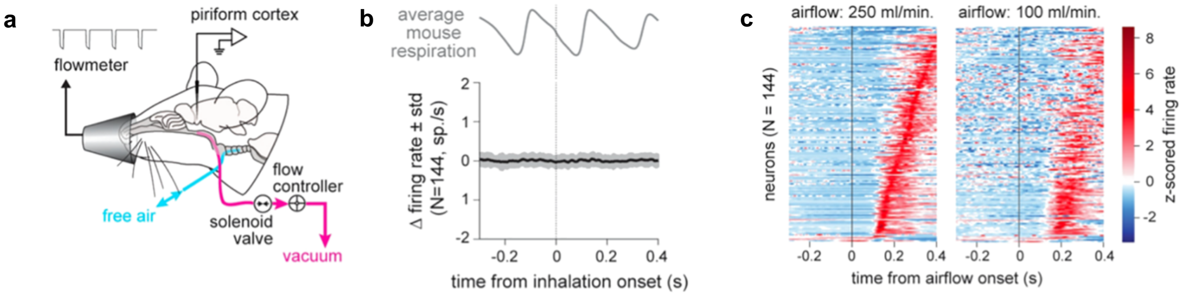

Figure 24. Tracheostomy preparation and loss of respiratory entrainment

(**a**) Schematic drawing of the experimental setup for artificial airflow stimulation of the nasal cavity in tracheostomized mice. (**b**) Grand-average PETH aligned to the self-generated inhalation onset (n = 144 neurons responsive to nasal airflow stimulation, n = 3 mice). Mean ± SEM is reported. Self-generated inhalations were detected using a piezo sensor embedded in a chest belt. (**c**) Raster maps of PETHs in tracheostomized mice aligned to the onset of the airflow pulse. (n = 144 neurons, n = 3 mice). PETHs were sorted bottom-up based on the latency to the peak of the response to the 250 ml/min airflow pulse.

To experimentally mimic the effect of respiratory events in the tracheotomized preparation, a set of airflow pulses of 150ms at different airflow rates was applied via a vacuum system connected to the nasopharynx. Five different airflow rates were tested, taking care to have comparable rates with physiological respiratory rates. Of the recorded neurons, 57.1% responded to the airflow stimuli. Additionally, these neurons exhibited varying response latencies that were stable across different airflow rates (Figure 24c) and distinct tuning curve properties (Figure 25). A fraction of responsive neurons increased their firing rate with increasing airflow, displaying a positive slope in their tuning curves, while others behaved in the opposite trend (Figure 25d). The results of the artificial stimulations were confirmed in awake, normally breathing control mice. To compare the artificial inhalation results with normally breathing mice, the distribution of airflow peaks was calculated at every inhalation and divided into ten equally populated bins; the mean amplitude of the spiking activity during each inhalation was then calculated for every neuron (Figure 26). Similar to what was found in the tracheotomized mice, also in normally breathing mice, some neurons showed increased response amplitude with faster inhalation speeds (36.7%), while others showed a decrease (41.7%).

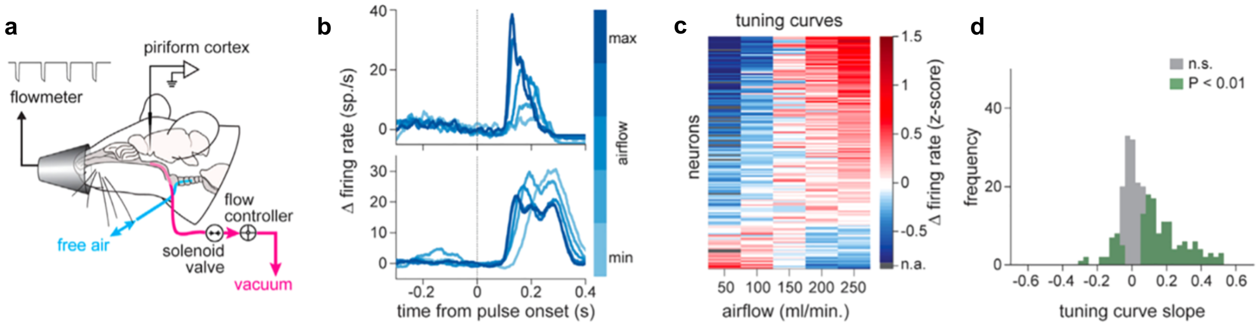

Figure 25. Airflow tuning curves upon artificial inhalations

(**a**) Schematic drawing of the experimental setup for artificial airflow stimulation of the nasal cavity in tracheostomized mice. (**b**) PETHs of two example neurons responding to five different airflow rates. (**c**) Raster map of airflow rate tuning curves (n = 144 airflow-tuned neurons of 252 neurons; n = 3 mice). (**d**) Distribution of the slopes of the airflow tuning curves. Shaded area, slopes significantly different from zero. Positive slope, 117 neurons; negative slope, 27 neurons (p < 0.01, t test).

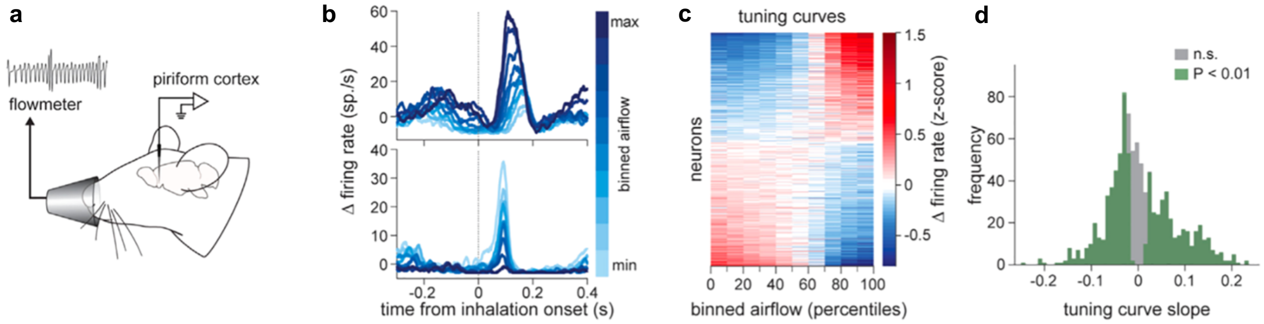

Figure 26. Airflow tuning curves in control mice

(**a**) Schematic drawing of the experimental setup for control recordings in the piriform cortex along with the recording of respiration. (**b**) PETHs of two example neurons responding to ten different peak airflow rates. (**c**) Raster map of peak airflow rate tuning curves (n = 748 peak-rate-tuned neurons of 955; n = 10 mice). (**d**) Distribution of the slopes of the tuning curves. Shaded area, slopes significantly different from zero. Positive slope, 350 neurons; negative slope, 398 neurons ($p < 0.01$, t test).

The above experiment suggests that the non-olfactory input originates from the nasal epithelium. However, the source of this non-olfactory input remains unknown. Interestingly, olfactory sensory neurons (OSNs) have been shown to function not only as odor detectors but also as mechanical sensors (Grosmaitre et al., 2007). This raises the intriguing possibility that OSNs could transmit both olfactory and non-olfactory information to the olfactory cortex via two independent channels. However, many odorants are also known to stimulate the trigeminal nerve. For instance, vinegar has both a smell detected by olfactory receptors and a pungent sensation detected by trigeminal receptors. Therefore, it cannot be excluded that the non-olfactory input is conveyed to the piriform cortex via this alternative channel. More specifically, a branch of the trigeminal nerve called the anterior ethmoidal nerve (AEN) innervates both the olfactory epithelium and the olfactory bulbs and is known to be sensitive to both chemical and mechanical stimulation (Maurer et al., 2019). Thus, an experiment was performed where the AEN was sectioned (see methods section: Surgical procedures for *in Vivo* extracellular recordings), and the neural activity in the piriform cortex was recorded. Disrupting the AEN left the tuning curve properties of neurons in the piriform cortex intact, excluding the possibility that the AEN might be the unique channel through which mechanosensory information is sent to the piriform cortex (Figure 27). Overall, these experiments indicate that neurons in the piriform cortex encode the airflow rate thanks to a mechanosensory input that is likely originating from the OSNs in the olfactory epithelium.

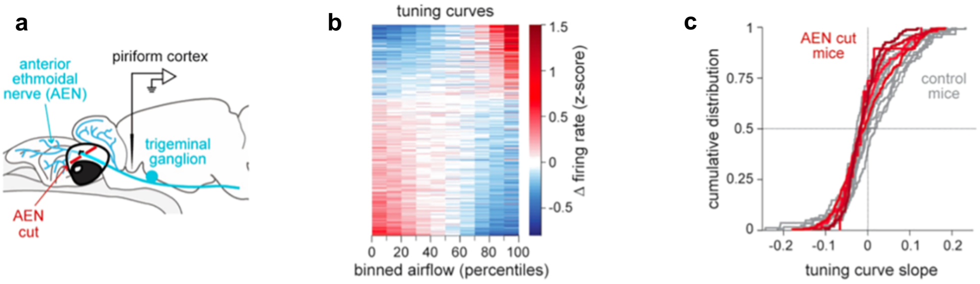

Figure 27. Anterior Ethmoidal Nerve (AEN) neurectomy experiment

(**a**) Schematic drawing of the AEN neurectomy experiment. (**b**) Raster map of the peak airflow velocity tuning curves after severing the AEN (n = 551 velocity-tuned neurons of 752; n = 5 mice). (**c**) Cumulative distributions of the tuning curve slopes in control and neurectomized mice.

Arousal State Signals and their Role in Sniffing Dynamics

The classification of respiratory events into fast and slow inhalations has allowed us to dissect and understand that the olfactory cortex represents the airflow information coming from the nostrils. However, on top of this basic physiologic parameter (i.e., respiratory velocity), there is another layer of complexity; indeed, faster inhalations, often referred to as sniffs, come in bouts that are known to be correlated with arousal and active exploration of the environment (Kepecs et al., 2006; Wachowiak, 2011). It is thus very likely that during a sniff, even in the absence of an odor stimulus, a top-down input might be an extra factor in the equation that describes the activity of neurons in the piriform cortex.

To isolate this factor from the bottom-up inputs coming from the olfactory epithelium the olfactory bulbs were surgically removed (Figure 28a) (see methods section: Surgical procedures for *in Vivo* extracellular recordings), allowing to better dissect the dynamics of arousal in the activity of neurons in the piriform cortex in an awake mouse. Remarkably, mice recovered fast from the surgery and showed a respiratory pattern similar to control mice (Figure 28b). Importantly, no odor responses were detected in the activity of piriform cortical neurons (Figure 28c). Another confirmation of the complete removal of bottom-up inputs from the olfactory epithelium comes from the fact that it was not possible to decode neither the phase nor the speed of the respiratory events from the activity of the neural population in the piriform cortex (Figure 29).

Figure 28. Bulbectomized mice stop responding to odors

(**a**) Example of coronal sections showing the complete removal of the olfactory bulbs. (**b**) Example raster plot showing a recorded population of neurons along with the respiratory trace of the mouse, inspiratory events are color coded as slow (green) and fast (purple) inhalations, see the text below for the classification pipeline. Shaded area is the odor period (5 s). (**c**) average PETHs of all neurons in control (top; 660 neurons; n = 6 mice) and bulbectomized mice (bottom; 153 neurons; n = 4 mice). Shaded area in grey is the odor period (5 s). Mean ± SEM are reported.

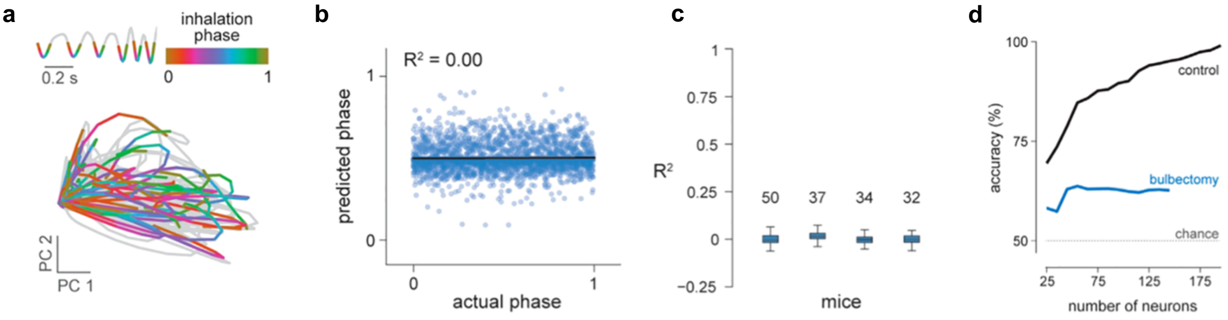

Figure 29. Inhalation phase decoding in bulbectomized mice

(**a**) Plot showing the first two principal components of neural population trajectories during individual respiratory cycles of an example mouse. Only the inhalation phase is color-coded, while the exhalation is grey. (**b**) Scatter plot showing the actual and predicted inhalation phase for an example mouse (n = 50 neurons), every point in the plot is the neural population PCA embedding in a time bin of 10ms for every phase of the inhalation. The actual inhalation phase was spanned from 0 (inhalation onset) to 1 (inhalation offset). (**c**) Plot showing on the Y axes the goodness of prediction (R^2) using the neural trajectories for every mouse (blue). The number of neurons for every mouse is indicated above each boxplot. (**d**) A linear support vector machine (lSVM) decoding accuracy of the inhalation speed as a function of the number of neurons.

Nonetheless, even in the absence of inhalation phase, speed and odor information a fraction of neurons (15.7%) was still responding to sniffs when aligned to the first sniff of an isolated sniffing bout (Figure 30a, b). However, the responses in bulbectomized mice were different compared to controls. In particular, the fraction of neurons that were responsive to sniffs halved (29.7% of neurons in control mice showed increased activity to sniffs), and of this, half of the responses were lower in amplitude and higher in their variability across sniffing bouts (Figure 31). This supports the idea that a big fraction of the respiratory-related responses in the piriform cortex indeed come from a bottom-up input, while suggesting that there is still a fraction that might depend on the internal state of the animal.

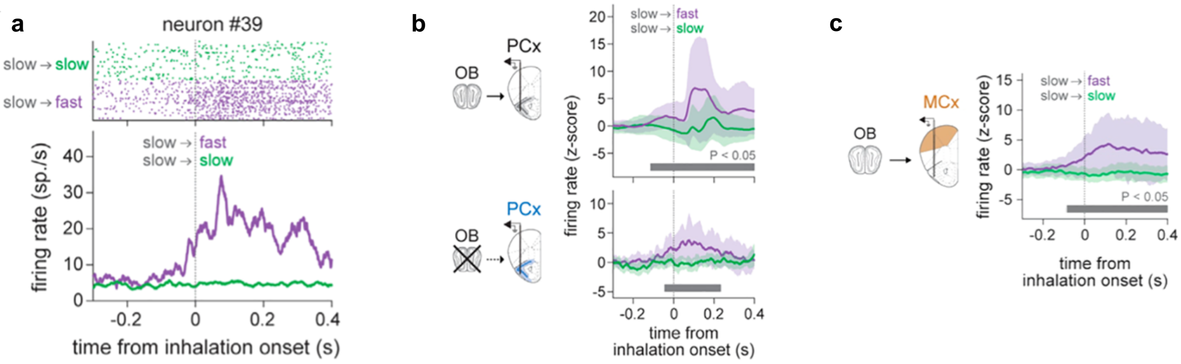

Figure 30. Neural responses associated with sniffing bouts

(**a**) Raster and PSTH of an example neuron after bulbectomy. The responses to the first sniff after at least five slow inhalations and to a slow inhalation are color-coded in purple and green, respectively. (**b**) Average PETHs of neurons preferring a sniff over a slow inhalation in control mice (top; 284 of 955 neurons; n = 10 mice) and in bulbectomized mice (bottom; 23 of 153 neurons; n = 4 mice). Shaded area, mean ± SEM. Grey bars indicate when the sniff responses are significantly bigger than the responses to a regular inhalation (Benjamini-Hochberg adjusted $p < 0.05$, one-sided t-test). (**c**) Average PETHs of motor cortex (MCx) neurons preferring a sniff over a slow inhalation in control mice (94 of 548 neurons; t-test, P-value < 0.01). Shaded area, mean ± SEM. The bar below the PETH indicates when the sniff responses are significantly bigger than the slow inhalation responses (Benjamini-Hochberg adjusted P -value < 0.05, one-sided t-test).

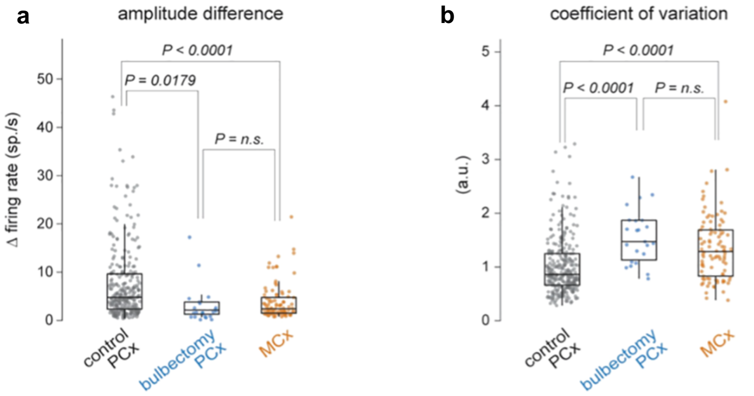

Figure 31. Quantification of neural responses to sniffs

(**a**) Difference between the amplitudes of the responses to the first sniff and a regular inhalation in the piriform cortex (PCx) of control and bulbectomized mice and in the MCx of control mice (P-value < 0.0001, one-way ANOVA; Tukey-Kramer post hoc P-values shown). (**b**) Coefficient of variation of the response amplitude across first sniffs in the PCx of control and bulbectomized mice and in the MCx of control mice (P-value < 0.0001, one-way ANOVA; Tukey-Kramer post hoc P-values shown).

Most importantly, the rise in the firing rate observed starts several milliseconds before the actual beginning of the fast inhalation (Figure 30a, b), suggesting a mechanism different from a mechanosensory input coming from the epithelium. Intriguingly, the leftovers of the responses to sniffs in bulbectomized mice are comparable to the responses of neurons in the motor cortex of control mice (Figure 30c and Figure 31), further suggesting a global cortical activation correlated with sniffing bouts. Overall, these data suggest that respiratory-modulated activity in the piriform cortex is driven by multiple independent factors, including a strong mechanosensory signal from OSNs and a more global, arousal-dependent cortical modulation that looks to precede the beginning of a sniffing bout. The top-down signal observed, whether coming from an arousal-dependent signal, from neuromodulators, or other channels, looks to have a temporal dynamic that goes beyond the single inspiratory event. Such signal might influence the representation of odor information by adding an additional layer of complexity to the output of the piriform cortex and might be interesting to further study how odor representation is altered by internal states.

Orthogonal Representation of Odor and Inhalation Information

Of the odor-responsive neurons recorded in the piriform cortex 72.2% (148 of 205 neurons) showed a modulation in their response amplitude during different inhalation types (fast *vs* slow) (Figure 18b). As described by the GLM model, the sensitivity to odor and inhalation information were heterogeneous across the neural population, showing a low interaction term between the independent variables. In other words, when modeling the activity of a neuron in the piriform with the equation below (Figure 32), taking in consideration the inhalation speed ($\alpha_i I$), the concentration of an odorant ($\beta_i C$) and their interaction ($\gamma_i IC$) the observed responses across neurons have shown to be uncorrelated (Figure 22).

$$r_i = r_0 + \alpha_i I + \beta_i C + \gamma_i IC$$

Figure 32. Model to predict neuron's firing

This equation was built to describe the activity of a neuron in response to a given odor concentration and inhalation speed. r_i is the firing rate of a cell. r_0 term represents its baseline activity. $\alpha_i I$ term is the fraction of response that describes the inhalation speed; I can be either 0 for slow or 1 for fast inhalations, α is the regressor weight for the inhalation term. $\beta_i C$ term is the fraction of response that describes the odor concentration; C is the logarithm of the three odor concentrations 0.01, 0.1 and 1% v./v., β is the regressor weight for the concentration term. $\gamma_i IC$ is the fraction of response that describes the interaction between the Inhalation and Concentration terms.

This feature enables the population to represent the two modalities in independent dimensions, indeed, when applying principal component analysis (PCA) on a pseudo-population of 464 neurons, giving as input a matrix of firing rates built with the average firing rate of every neuron (using a 180ms window starting from the inhalation onset) during different respiratory events (8 conditions: no odor during slow and fast inhalations and odor responses at three different concentrations during slow and fast inhalations) showed that the inhalation speed and odor concentration information where represented onto orthogonal dimensions (Figure 33). By looking at the two principal components of the pseudo-population, it is clear that the first one represents the inhalation speed information, while the second principal component represents the presence/absence of odor along with its concentration. This suggests that the two pieces of information are not affecting each other, meaning that a change in inhalation speed is not affecting the dimension that represents odor concentration and vice-versa for a shift in the odor concentration dimension. Such observation was quantified thanks to linear support vector machine (lSVM) classifiers, trained to decode either the odor concentration or the inhalation speed only by using the projections of neural activity of the first 15 PCs, one after the other (Figure 34). As suggested by the graphical interpretation of Figure 33, lSVMs trained to decode inhalation speed reached good accuracy levels only in the first principal component while going at the chance level on the other dimensions. Conversely, when trying to decode odor concentration, it was not possible to do it in the first principal component, but good performance levels were reached in the second dimension (Figure 34a).

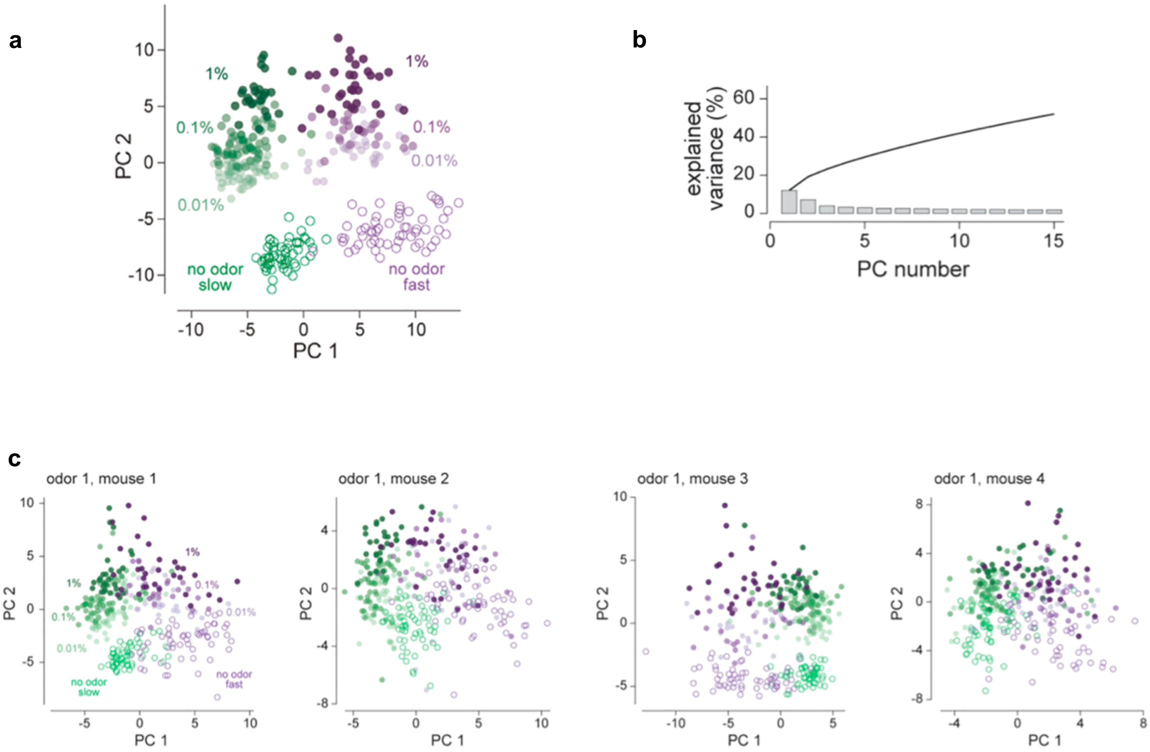

Figure 33. PCA of the population activity

(**a**) PCA embedding of pseudo-population responses (464 neurons, n = 4 mice) to three different concentrations of an example odor (eucalyptol) during slow (green) and fast (purple) inhalations. Each dot is a response in a 180ms window starting at inhalation onset. Empty dots represent inhalation responses in the absence of odors. A random sample of all responses is shown. (**b**) Variance explained by the first 15 PCs of the covariance matrix, obtained from the pseudo-population of top-left. (**c**) Same as top but for the 4 single mice with which was built the pseudo-population.

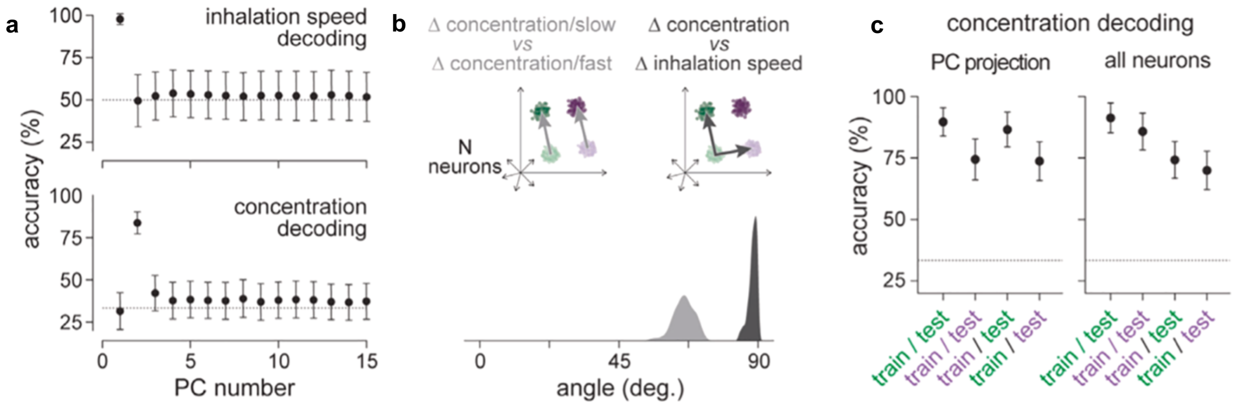

Figure 34. lSVM decoders applied on population activity

(**a**) Decoding accuracy of inhalation speed and odor concentration using the projection of the pseudo-population odor responses in figure 33 on each of the first 15 PCs. Mean ± SD is shown. (**b**) Angle between vector pairs representing concentration changes (light gray) and vector pairs representing a concentration change and an inhalation speed change (dark gray). (**c**) Concentration decoding accuracy of cis- and trans-decoders using the pseudo-population response projections onto the second and third PCs (PC projection). Concentration decoding accuracy of cis- and trans-decoders using non-reduced population responses (all neurons). Mean ± SD is shown. Slow inhalations (green) and fast inhalations (purple).

To further probe the orthogonality observed in the PCA analysis, a linear discriminant analysis (LDA) was applied to the multidimensional neuron response space to find the response vectors that best tell odor concentrations apart during slow or fast breathing (see methods section: Angle between encoding axes). When calculating the angle between the encoding vectors of a difference in concentration and inhalation speed, they distribute at 90°. In contrast, the encoding vectors of changes in odor concentration at two different inhalation speeds were nearly parallel (Figure 34b). Note that, in high-dimensional spaces, such as the analyzed neuron-response space, exact parallelism is rare due to the spread of vectors.

Both the low-dimensional embedding obtained from PCA analysis and the multidimensional response vectors obtained from LDA indicate that the representation of odor concentration decoded from the activity of the neural population in the piriform cortex might be invariant to sniffing. This suggests that the neural population can extract a perceptually stable representation of external odor concentration despite the variability introduced by respiratory sampling. To test this key point, lSVMs were trained to decode the odor concentration using either slow or fast inhalations as a training set. The decoders were then tested either on the same inhalation type of the training set (cis-decoding) or on the opposite inhalation type (trans-decoding). Two conditions of input data to the lSVMs were tested: (I) The second and third principal components of the low-dimensional embedding obtained from PCA which explained the concentration dimension (see Figure 34a); (II) the untransformed multidimensional neural responses. In both input data cases, the lSVMs reached good accuracy levels both in cis- and trans-decoding conditions (Figure 34c). Similar results were obtained using a smaller window to extract inhalation-aligned neural activity (Figure 35a, b) and using spike counts for concatenated 10ms or 10° bins over a respiratory cycle (Figure 35c).

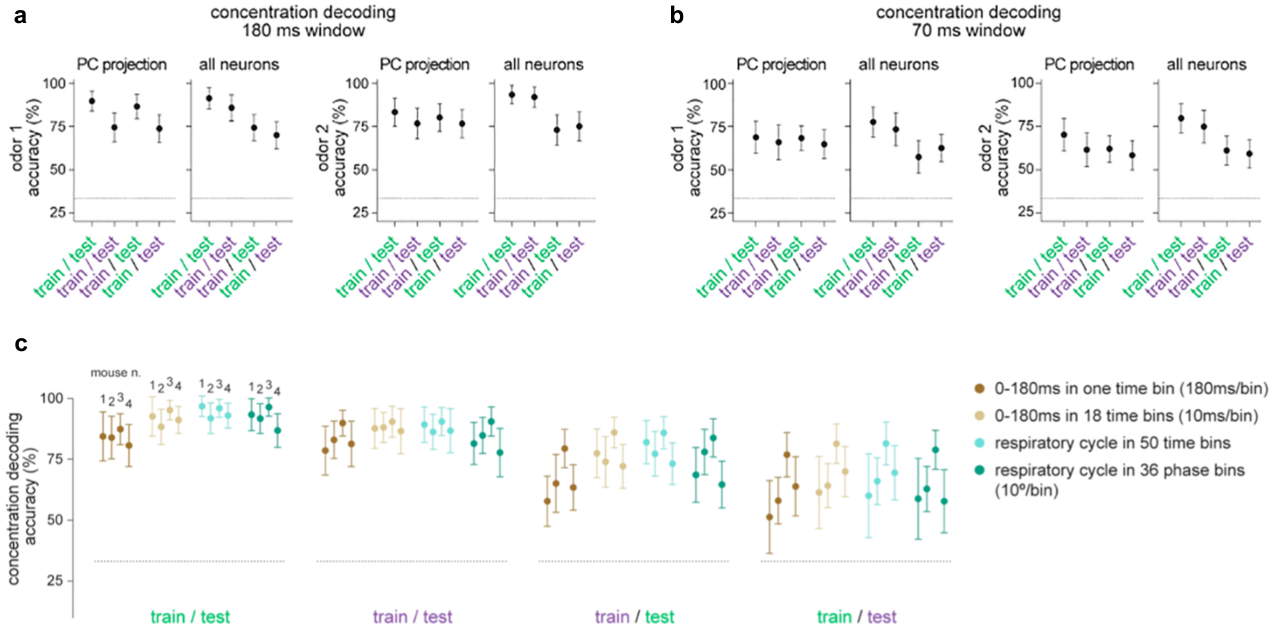

Figure 35. Different lSVM decoders applied on population activity

(**a**) Concentration decoding accuracy of cis- and trans-decoders using the pseudo-population response projections onto the second and third PCs (PC projection). Concentration decoding accuracy of cis- and trans-decoders using non-reduced population responses (all neurons). Mean ± SD is shown. Slow inhalations (green) and fast inhalations (purple). Odor 1 = eucalyptol, odor 2 = pinene. Concentration decoding was applied on a window of 180ms starting from inhalation onset. (**b**) same as in a but with a window of 70ms starting from inhalation onset. (**c**) Comparison of the accuracy of a linear decoder across four different coding schemes. Dark brown: average population activity in the 0-180ms window of a respiratory cycle; 0ms: inhalation onset. Light brown: neural population trajectory during the 0-180ms window; the neural activity during the 180ms window was binned in 18 bins of equal duration (10ms), and a population vector was built using the average activity of each neuron during a given time bin; finally, the 18 vectors were concatenated to obtain the population trajectory. Light teal: neural population trajectory during the entire respiratory cycle; the respiratory cycle was binned in 50 time-bins of equal duration within the cycle; the time bin duration varied across respiratory cycles due to the different duration of each cycle; the 50 population vectors were concatenated to obtain the population vector during a respiratory cycle. Dark teal: neural population trajectory during the entire respiratory cycle using the phase instead of the timing; the respiratory cycle was binned in 36 phase-bins of equal length (10°); the 36 population vectors were concatenated to obtain the population trajectory during a respiratory cycle. Mean ± standard deviation is shown for four mice.

The fact that both in cis- and trans-decoding, it is possible to extract the odor concentration information independently from the inhalation speed is an interesting feature of the neural population. To further dissect this characteristic and understand the contribution of different neurons, the population was split based on the α (inhalation speed) and β (odor concentration) regressor weights obtained from the GLM analysis (Figure 22). When selecting a subpopulation of either positively or negatively correlated neurons with the olfactory and non-olfactory inputs (i.e., correlated α and β coefficients) (see insets Figure 36a, respectively red and blue subpopulations) when testing lSVM in trans-decoding conditions, the performance was at chance level (Figure 36b). Only when combining positively and negatively correlated subpopulations producing an uncorrelated subpopulation was the lSVM able to stand beyond chance levels in trans-decoding conditions (Figure 36b). This is also visually observable in the structure that is produced by the uncorrelated subpopulation when plotting the first two principal components of the neural embedding (Figure 36a, black subpopulation).

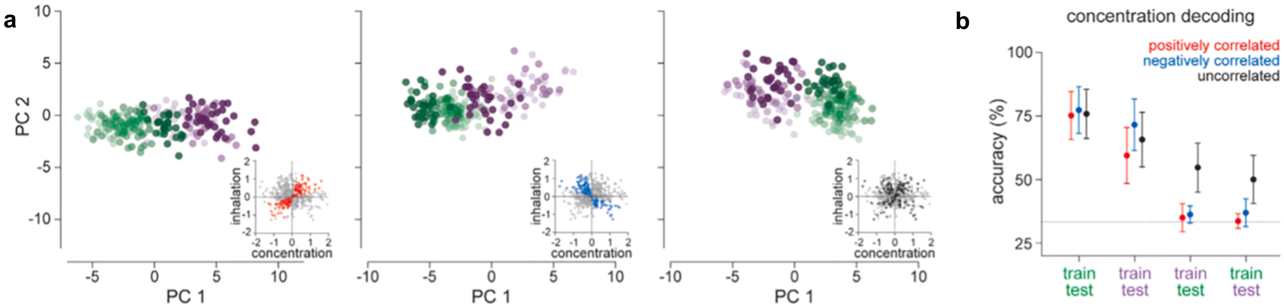

Figure 36. Decoding accuracy of correlated and uncorrelated pseudo-populations

(**a**) PCA embedding of concentration responses for three pseudo-populations with positive (left), negative (center), and no correlation (right) between inhalation and concentration sensitivity. Insets: scatterplots of inhalation and concentration regression coefficients for all the neurons of the same pseudo-population used in figure 33a. Red, neurons with positive correlation; blue, neurons with negative correlation; black, neurons without correlation. An equal number of neurons was randomly sampled from each sub-population (n = 143 neurons). A random sample of all responses is shown. (**b**) Concentration decoding accuracy of cis- and trans-decoders using the three neural sub-populations used in panel a. Mean ± SD is shown.

Another evident feature of the neural population is that a fraction of neurons had a very low α (inhalation speed) coefficient; these neurons are not influenced in their response by the inhalation speed. In other words, they are sniff-invariant and might alone carry the information necessary to read out external odor concentration independently from inhalation speed. Sniff-invariant neurons of the population were classified thanks to a linear regression model with concentration and inhalation speed regressors; those neurons that fell within 0 ± 0.75 standard deviations of the inhalation speed regressor coefficient were classified as such (Figure 37a, black subpopulation). Instead, an equal number of neurons with inhalation speed regressor beyond ± 1.75 standard deviations were classified as mechanosensitive neurons (Figure 37a, orange subpopulation). Interestingly, the mechanosensitive subpopulation carried a similar amount of information. Indeed, an ISVM trans-decoder trained and tested on the mechanosensitive subpopulation reached similar performances to the ISVM that used the sniff-invariant subpopulation (Figure 37b). Moreover, when feeding ISVMs with neural activity calculated on 10ms bins of the first 200ms of the inhalations, the accuracy of the decoders for both sniff-invariant and mechanosensitive subpopulations was still equal (Figure 37c), ruling out the possibility of an information difference in the temporal domain of the single inspiratory event. From the experiments performed, it is, however, not possible to assess the effective downstream readout of the information carried by the two different subpopulations.

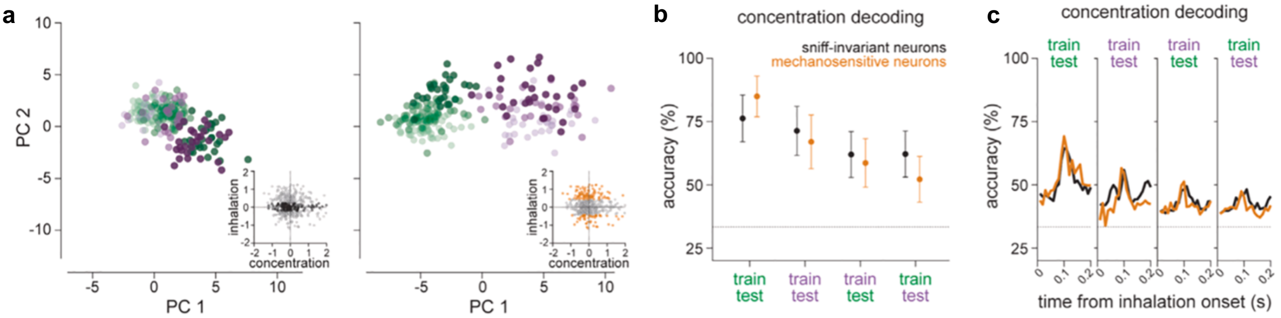

Figure 37. Decoding accuracy of sniff-invariant and mechanosensitive pseudo-populations

(**a**) PCA embeddings of concentration responses using a pseudo-population with (left) and without (right) sniff-invariant neurons. Insets: scatterplots of the inhalation and concentration regression coefficients for all the neurons of the same pseudo-population used in in figure 33a. The subset of neurons in the population response vector is highlighted by color: black, sniff-invariant neurons; orange, mechanosensitive neurons. An equal number of neurons was randomly sampled from each sub-population (n = 143 neurons). A random sample of all responses is shown. (**b**) Concentration decoding accuracy of cis- and trans-decoders inhalation speed using sniff-invariant (black) and mechanosensitive (orange) neurons. Mean ± SD is shown. (**c**) Concentration decoding accuracy within and across inhalation speed over the time course of an inhalation ($p > 0.05$; two-way ANOVA). An equal number of neurons was randomly sampled from each sub-population (n = 143 neurons).

Together, these results show that is the uncorrelation of inhalation speed and odor concentration sensitivities among neurons that allows the population in the piriform cortex to become sniff-invariant. Moreover, the sniff-invariant information is homogenously spread among all odor-responsive neurons and do not depend on their mechanosensitivity.

Role of Airflow Signals in Stabilizing Perception Against Flow-Dependent Concentration Fluctuations

When comparing the principal component embedding of the sniff-invariant and mechanosensitive pseudo-populations (Figure 37a), it can be observed that, due to the orthogonal representation of inhalation speed, the mechanosensitive pseudo-population (orange) spreads odor concentration information across two dimensions, rather than just one dimension as is the case for the sniff-invariant subpopulation (black). This feature might allow the neural population to disentangle better the fluctuations of the external odor concentration from the fluctuations driven by changes in inhalation speed. This possibility is depicted in Figure 38, where is shown an example of 2 neurons sensitive only to odor concentration or also with an orthogonal mechanosensory component. Adding the mechanosensory input in this example separates the perturbation component that is induced by a change in inhalation speed, allowing an improved concentration discrimination boundary.

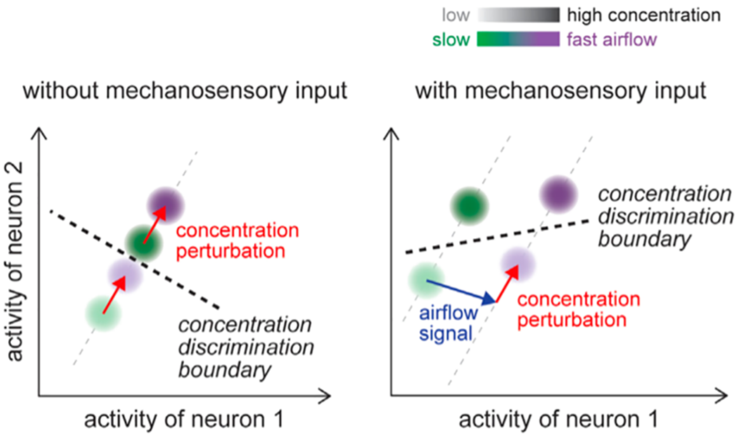

Figure 38. Toy models of two neurons with and without mechanosensory input sensitivity
Example of how adding an independent mechanosensory signal distinguishes the inhalation-induced concentration fluctuation from an inhalation-independent change in concentration.

To test this possibility, both scenarios were simulated, producing distributions of neural population responses with different levels of inhalation speed-dependent concentration change and mechanosensory input. These synthetic data were generated by determining the weights for odor and inhalation covariates from a linear regression model applied to recorded neural responses. Various levels of interaction between airflow and odorant deposition were modeled by assuming that the inhalation-driven change in concentration (ΔIC) is proportional to both the initial concentration and the inhalation speed, following previous fluid dynamics models (Shusterman et al., 2018) (see methods section: Simulation of sniff-induced concentration changes). When looking at the neural embedding of the simulated neural responses is clear that the odor concentration representation is more ambiguous when the mechanosensory component is missing (Figure 39).

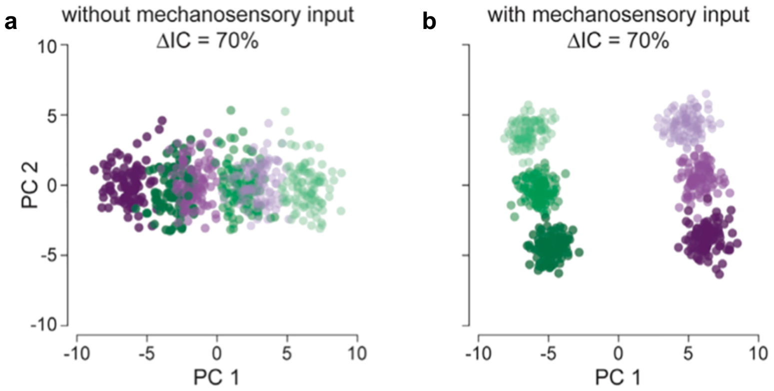

Figure 39. Inferred effect of the mechanosensory input on the concentration representation in the presence of an inhalation-driven alteration of the odor concentration.

(**a**) PCA embedding of population concentration responses with a 70% inhalation-driven concentration change (ΔIC) and without inhalation input. (**b**) PCA embedding of population concentration responses with a 70% ΔIC and mechanosensory input.

Indeed, when training ISVM decoders without the mechanosensory component, a drop in the performance when decoding a different inhalation speed was observed in correlation with an increase in the effect of inhalation-driven change in concentration (ΔIC) (Figure 40). This performance drop was not observed when adding the mechanosensory component to the simulated neural population responses. Overall, these data suggest that representing inhalation speed information in an orthogonal dimension is critical to handling the effects of respiration on the deposition of odor molecules on the olfactory epithelium.

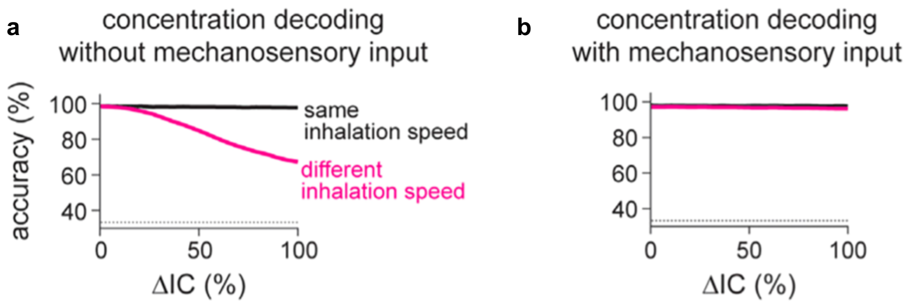

Figure 40. ISVM decoders with and without mechanosensory input

(**a**) Concentration decoding accuracy for increasing levels of inhalation-dependent ΔIC without mechanosensory input within (black) or across (magenta) different inhalation speeds. (**b**) Concentration decoding accuracy for increasing levels of inhalation-dependent ΔIC with mechanosensory input within (black) or across (magenta) different inhalation speeds.

DISCUSSION

The experiments and analyses presented reveal a distributed representation within the anterior piriform cortex, encompassing both olfactory and respiratory information. A significant number of neurons respond to both types of external stimuli, making it challenging for any single neuron to accurately extract the precise external odor concentration. However, it is important to note that individual neurons do not operate in isolation; they are part of a larger network. When we shift our focus from the level of individual neurons to a population perspective, an interesting phenomenon emerges. The combined, uncorrelated sensitivities of the neuronal population to both sensory stimuli introduce an additional layer of information. This suggests that while single neurons may struggle to distinguish specific odor concentrations, the collective behavior of the neural population can accurately process and respond to complex sensory inputs. Also, it is very likely that the inhalation speed information is sent to neurons in the piriform cortex via the olfactory bulbs directly from the peripheral sensory organ, thanks to OSNs' ability to not only express olfactory receptors but also mechanosensory ones (Connelly et al., 2015; Grosmaitre et al., 2007).

Even if the population in the piriform cortex can extract external odor concentration despite fluctuations in the respiratory velocity, it cannot be excluded that such separation of information happens already at the level of the olfactory epithelium. For instance, it has been shown that by employing fluid-dynamics simulations of both airflow and odorant deposition comparing sniffing *vs* quiet breathing in the nasal cavities of coyote (*Canis latrans*), the amount of air that reaches olfactory regions increases during sniffing. Also, the distribution pattern of odorant deposition changes according to the respiration type and the type of molecule (Rygg et al., 2017) (Figure 41).

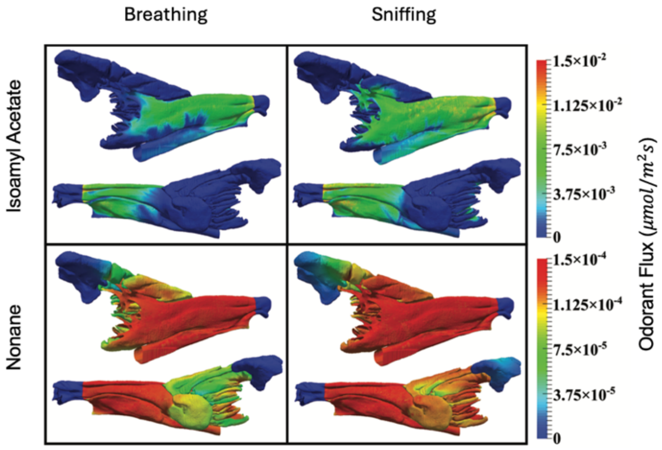

Figure 41. Reconstructions of coyote nasal cavity during odor presentation at different inhalation speeds
Contours of odorant flux for isoamyl acetate, and nonane during inspiration at quasi-steady flow rates corresponding to quiet breathing (4.34 L/min) and a notional quasi-steady sniff (8.88 L/min) with an inlet odorant concentration of 1 μmol/m^3. Odorant flux contours on the airway walls are shown from a medial (top) and lateral (bottom) perspective in each panel. Figure taken from Rygg et al., 2017.

This suggests a potential mechanism already at the level of olfactory epithelium based on anatomical segregation. The responses during slow, regular breathing activate a specific pattern of OSNs, which is different when the animal sniffs. In that way, two potentially partially overlapping populations of OSNs respond to the same odor but at different respiratory velocities. These two subpopulations, even though projecting to the same glomerulus, might differentially impact the output of that glomerulus.

Another reasonable model with which airflow information might be extracted from the OSNs independently from odor output might rely on the fact that around 50% of the OSNs respond to mechanosensory stimuli (Grosmaitre et al., 2007), while only a few respond to a specific odor molecule. In that way, the airflow information might be extracted from the overall OSN population, and the variability introduced by the few odor-responsive OSNs might be filtered out. It has been shown that different glomeruli in the olfactory bulbs display an oscillatory activity that is coupled with the respiratory phase. Such phase-locked activity was shown to be invariant to changes in airflow speed and showed phase shifts upon odor stimulation. Interestingly, such observed phase shifts were demonstrated to be concentration invariant (Iwata et al., 2017). However, it is not clear whether mechanosensory and olfactory information will reach the olfactory bulb as parallel and independent streams of information. Given the observed mixed responses in the piriform cortex, this would imply that they are mixed at a later stage of brain processing.

Other variables come into play that further complicate the prediction of the external odor concentration; such variables have a different impact depending on the odor molecule: temperature, humidity, size, and shape of the molecule, solubility of the molecule into the mucus, affinity of the molecule to the olfactory receptor, presence of other odor molecules that alter the above parameters. The experiments in the results section analyzed a simplified model, where only monomolecular odorants were presented at a steady concentration, to dissect the effect of respiratory velocity on a stable condition. However, in a natural context, odors diffuse in the air with fluctuation profiles in odor concentration, mostly depending on the distance from the odor source, molecular characteristics of the odor, wind speed, and wind direction. A typical profile of a distant odor source is composed of odor plumes that show temporal profiles with peaks of odor concertation alternated to lower concentrations and absence of odor (Reddy et al., 2022) (Figure 42).

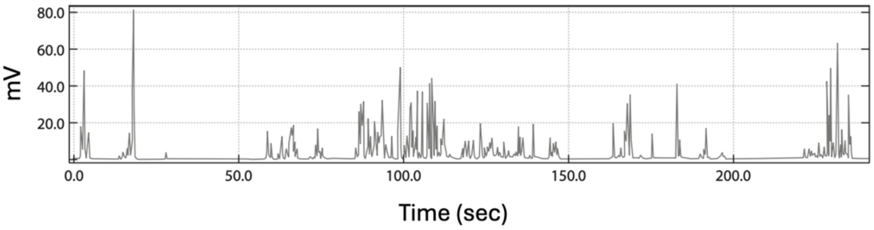

Figure 42. Concentration profile of a distant odor
Propylene odor profile measured 50m away from the source. The plot shows 4 minutes of data, is clear the intermittent clustering of odor plumes. Figure modified from (Reddy et al., 2022).

Animals, however, developed efficient ways to deal with such complex data and extract relevant information. Gire et al., 2016 showed that mice employ different strategies to find an odor source location according to their knowledge of the environment. Mice track odor plumes to find the correct reward location when the source is not known, when instead the location is memorized, they shift to a more efficient and stereotyped strategy. Experience thus affects the way mice use environmental information in a flexible way. The act of sniffing is, however, used by mice to further improve sensory perception and odor-source location when necessary, and it has been shown to be synchronized with nose movements when tracking an odor source (Findley et al., 2021).

Importantly, an assumption made so far is that knowing the real external odor concentration during every respiratory sample is a relevant feature. However, in many natural contexts, the change in concentration over time, rather than the absolute concentration at any given moment, might be more relevant. For example, an increasing odor concentration could indicate that an animal is getting closer to a source, which might be more valuable information than the precise concentration at any moment. Animals might rely more on trends or patterns in odor concentration rather than needing to know the exact concentration at each inhalation. This suggests that the relative difference in odor concentration across respiratory cycles or between nostrils might be more critical than the absolute concentration. In nature, odor concentrations fluctuate due to varying environmental factors; given this variability, organisms may have evolved to rely on a broader interpretation of olfactory cues rather than precise concentration measurements, which could be less reliable or not necessarily the most relevant information.

The data shown point to the fact that it is the respiratory variability by itself that introduces fluctuations in the acquisition of olfactory information; these fluctuations can create noise in the sensory input, making it challenging for the system to accurately interpret the external odor environment. Neural circuits might however integrate information over multiple respiratory cycles, averaging out the fluctuations to extract a more stable odor signal. This would reduce the noise introduced by any single inhalation. On the other side, behavioral studies has also shown that rats can take correct decisions within the fast interval of a single sniff (Uchida and Mainen, 2003). This cannot exclude the possibility of integrating over time to denoise variability introduced by respiratory sampling, suggesting that multiple mechanisms might coexist as a function of the specific problem to solve. For instance, you can immediately spot a freshly cooked cake inside a room using your eyes, but it will take quite some time to do the same, only with your nose. The need for temporal integration in the olfactory world is thus critical in specific contexts: in the piriform cortex, it was shown that it is possible to decode the time from the onset of an odor for several seconds after the odor stimulus is switched off; also, this feature was partially disrupted when impairing the recurrent activity in the piriform with tetanus toxin (Figure 43) (Bolding et al., 2020). This suggests the interesting hypothesis that the olfactory cortex might work as a clock that keeps track of the last time an odor was encountered; such information might be employed to improve olfactory navigation. For example, even if odor plumes are complex stimuli, they still hold predictable statistical features, knowing the inter-plume interval might be a valuable information to estimate the distance from the odor source.

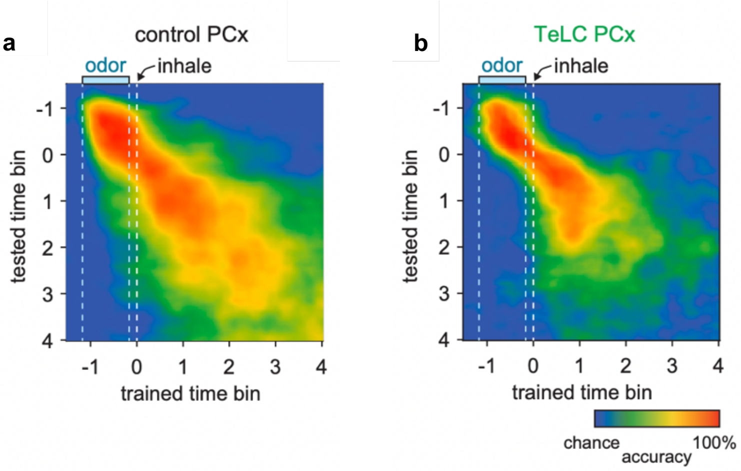

Figure 43. Temporal coding in the piriform cortex
(**a**) Averaged cross-time decoding from a pseudopopulation of 200 cells, both for control and tetanus toxin (TeLC) infected mice. (**b**) Same as right but for TeLC mice. Figure taken from (Bolding et al., 2020).

Regarding the coexistence of multiple mechanisms, it is clear that both the olfactory bulbs (Shusterman et al., 2011; Smear et al., 2011; Spors and Grinvald, 2002) and the piriform cortex (Bolding and Franks, 2017) represent the phase of respiration. It has been proposed in the piriform cortex that, according to the type of information to extract, the information phase might be more relevant. When asking a decoder to classify odor identity, the best accuracy was fastly reached within less than 100msec; instead, for odor concentration, the accuracy level increased over time, suggesting an integration mechanism through the single respiratory cycle (Bolding and Franks, 2017). It is also important to note that respiration is not only relevant for decoding odors; it has multiple functions that are not directly related to the olfactory dimension. Respiration-entrained rhythms are widespread in the brain and, for instance, might aid communication between brain areas (Tort et al., 2018).

The variability in sensory sampling introduced by breathing patterns can, however, be used from the population in the piriform cortex as a feature to extract the external odor concentration. This hypothesis might rely on the uncorrelated sensitivities of single cortical neurons to the two different sensory inputs. This solution is different from the canonical corollary discharge, where a copy of the motor command is sent to sensory systems to allow for the subsequent disambiguation (Crapse and Sommer, 2008). Here, is the emergent property of the neural population that generates an improved sensory representation. It has also been previously shown that neural populations can represent various dimensions of behavior, such as movement, planning, and attention, simultaneously and independently. Such representation allows the brain to process complex information without interference from concurrent activities. This multidimensional activity reflects the brain's ability to encode a wide range of internal and external variables in an orthogonal manner, ensuring that each behavior or state is associated with a distinct neural signature (Stringer et al., 2019).

Recently, it was also shown that neurons in the primary visual cortex show uncorrelated responses to saccades and visual inputs. In this case, an input from the pulvinar signals the beginning of a saccade in the visual cortex. When a saccade occurs, the direction selectivity of neurons in the visual cortex is “scrambled” thanks to this pulvinar input; this was proposed to be the mechanism thanks to which image representation during saccades does not deteriorate (Miura and Scanziani, 2022). This strategy looks to be different from the one observed here in the olfactory system. However, is to be noted that filtering out few samples during a saccade from a system that acquires visual data at around 50Hz in mice might have a lower impact on visual behaviors compared to the olfactory system where, if we assume that olfactory sampling goes at the frequency of respiration, it peaks with sniffs at 15Hz. Plus, there is a substantial difference between the consequence of a saccade (i.e., a fast and homogeneous movement of the sensory world on the retina) and the consequence of a sniff (as discussed before, see Figure 41).

An open question is whether specific cell types are responsible more than others for the uncorrelated responses observed. Indeed, with extracellular recordings, it is challenging to identify cell types, as only the features extracted from the waveforms can be used to classify different neuronal types. There were no significant differences when trying to classify regular spiking from fast-spiking neurons from their waveform features and firing rates (see Results section, Figure 23). To address the issue of cell identification, a first option would be to perform similar experiments shown in the results section but contemporarily optically tag different genetic types of cells by means of optogenetics (Kvitsiani et al., 2013) to dissect their differential involvement. However, the sniff-invariant representation of odor concentration was shown to be homogeneously spread among the population of recorded neurons, at least in terms of α and β coefficients of the GLM model (see Figure 37), pointing towards a shared representation of the sensory-motor features.

On the other side, the behavioral relevance of the population-level orthogonality remained unexplored. It is still not known whether and how the mouse employs such information. What is missing is a loss of function experiment where the respiratory velocity is uncoupled from the external odor concentration. To do so, optogenetics might be used to induce artificial odor stimulations; this technique is already established and involves the optogenetic stimulation of the olfactory bulbs (Chong et al., 2020; Zhu et al., 2021). Such an approach would allow to experimentally manipulate odor perception but uncoupling the respiratory velocity with the concentration information. Does this disrupt the orthogonality observed at the population level? Genetic models that disrupt mechanosensory sensitivity might be employed, as shown with the CNG2A knock-out mice (Grosmaitre et al., 2007).

It has been shown that the performance of a mouse in a concentration discrimination go no-go task is not affected by the respiratory velocity (Jordan et al., 2018b), similarly, also humans are able to guess odor concentration independently from respiratory velocity (Teghtsoonian and Teghtsoonian, 1978). It can be hypothesized that throughout experience there is a learned link between the consequence of a specific respiratory velocity and the prediction of the sensory stimulus. What would happen if this learned link is disrupted?

For instance, it has been shown in the visual cortex that sensory-motor coupling produces a specific balance between excitation and inhibition in the visual cortex that shapes behavior. Here, excitatory locomotor and inhibitory visual inputs are built over time by visuomotor experience. When artificially uncoupled (a mismatch of the optic flow is produced when the animal is moving in a virtual reality environment), somatostatin-expressing cells are transiently releasing from inhibition excitatory pyramidal neurons to signal an unexpected mismatch between locomotor and visual inputs. Such experience-dependent mechanism allows the visual cortex to correctly disentangle external visual sensory stimuli from locomotory-produced movements of the visual world in an adaptive manner (Attinger et al., 2017). Similarly, the olfactory cortex also deals with sensory-motor integration, where olfactory stimuli are coupled with respiratory signals. It would be interesting to understand whether an archicortex like the piriform cortex deals with this kind of experience-dependent feedback similarly to neocortical areas.

Finally, the whole project was conducted on head-fixed mice, and while this approach has the advantage of precise control over stimuli, it comes with the drawback of simplifying naturalistic behaviors. For instance, a common example of an olfactory task in the real world is the odor-source location (Crimaldi et al., 2022; Reddy et al., 2022). Mice show a rich behavioral repertoire when tracking odor sources encompassing nose and head movements (Findley et al., 2021), as well as inter-hemispheric communication (Esquivelzeta Rabell et al., 2017). On top of behavioral complexity, stimulus complexity also increases, with odorant diffusion following fluid dynamics rules that are hard to predict. It is reasonable to hypothesize that behavior evolved specifically to solve these complex and ethologically relevant tasks; it will be critical in the future to understand how these different variables are integrated into the equations that describe olfactory behaviors, where respiratory velocity is only one of them.

METHODS

Experimental Model and Study Details

Mice

All experimental manipulations were performed according to Italian legislation (DL 26/214, EU 63/2010, Ministero Della Sanita`, Roma) and FELASA recommendations for the care and use of laboratory animals. Animal research protocols were reviewed and consented to by the Italian Ministry of Health. We used 6-9 weeks old C57BL/6J mice of both sexes (Jackson Laboratory, RRID:IMSR_JAX:000664). Mice were co-housed with their littermates (2-4/cage) and maintained on a 12hr/12hr light/dark cycle at room temperature (20-22°C), 40-60% humidity, with food and water *ad libitum*. Littermates were randomly assigned to experimental groups. Males and females were randomly assigned. Four C57BL/6 mice were used for the two odors/three concentrations (0.01, 0.1, and 1% v./v.) experiments; two C57BL/6 mice were used for the five odors/two concentrations (0.01 and 0.1% v./v.) experiment; four C57BL/6 mice were used for the odor identity experiments, 5 odors delivered at one concentration (0.01%); three C57BL/6 mice were used for the artificial inhalation experiment; four C57BL/6 mice were used for the bulbectomy experiment; five C57BL/6 mice were used for the AEN neurectomy experiment. None of the mice was involved in other procedures. No analysis of the influence of sex on the results of the present study was conducted because it was not relevant to the scope of the study.

Surgical procedures for *in Vivo* extracellular recordings

Animals were anesthetized with isoflurane (3% induction, 1.5% maintenance) and placed on a custom-made feedback-controlled heating pad. Pre-operative analgesia was induced through intramuscular injection of a bolus (4ml/g) of carprofen (Rimadyl, 0.05%)/ dexamethasone (0.01%) and scalp infiltration of a tetracaine solution (0.05%). Post-operative analgesia was provided through carprofen diluted in the water bottle (Rimadyl, 134ml/100ml) following the procedure. Silicone-based eye ointment was applied on the eyes to protect the corneas during the surgery. Anesthetized mice were mounted in a stereotaxic frame. The scalp was shaved with shaving cream and cleaned with isopropyl alcohol and iodopovidone. The skin and the periosteum from the lambdoid to the frontonasal sutures were removed, and muscles were partially detached from the skull to expose the occipital bone and the parietal ridges. To increase adherence of the implant to the skull, superficial grooves were drilled in the frontal, parietal, interparietal, and occipital bones. After leveling the skull yaw, pitch, and roll to obtain a flat skull configuration, two small reference crosses were scored using a scalpel at bregma and at the entry point of the Neuropixels probe (AP: 2.0/2.1 mm; ML: -2.0/-2.1 mm from bregma), and the incisions were filled with surgical ink and covered with UV-curable acrylic (Optibond). Finally, a titanium headplate was mounted onto the arm of the stereotaxic manipulator and attached to the skull with cyanoacrylate (Loctite 454) and dental cement (Paladur). One day before the recording mice were anesthetized again and placed in the stereotaxic manipulator. Two small craniotomies were opened: one for probe insertion (AP: 2.0/2.1 mm; ML: -2.0/-2.1 mm from bregma) and the other over the contralateral posterior parietal cortex for the ground electrode. The dura mater was not removed. Finally, the two craniotomies were filled with surgical silicone (Kwik-Cast, WPI).

For tracheostomy experiments the electrophysiological recordings were performed immediately after the surgical preparation. For this procedure, mice were kept anesthetized throughout the surgical procedure and the recording with urethane (0.9 g/kg). Following a previously developed method (Eiting and Wachowiak, 2018), a cannula was placed into the nasopharynx via the upper part of the trachea to allow the artificial suction of air through the nasal cavity; another cannula was placed in the lower end of the trachea to allow the natural gas exchange with the lungs.

Somatosensory deafferentation was obtained by sectioning the anterior ethmoidal nerve (AEN) under isoflurane anesthesia before the recording session. The ocular bulb was laterally retracted, the upper region behind the eye was infiltrated with tetracaine solution (0.05%), and the nerve was cut by blunt dissection with fine forceps at the exit from the ethmoid foramen. The cut was verified post-mortem by visual inspection.

Olfactory deafferentation (bulbectomy) was obtained by aspirating the olfactory bulbs using a blunted needle attached to a vacuum system, while Ringer’s solution was continuously applied to cleanse the craniotomy site and remove all olfactory nerves down to the cribriform plate. The cavity was then filled with a sterile gelatin sponge (Gelfoam) and sealed with dental cement. Post-mortem verification of bulbectomy completeness was conducted by visually examining coronal brain sections, with any subjects displaying identifiable glomeruli being omitted from further analysis.

Habituation to the experimental rig

Mice were habituated to head-fixation and the experimental rig starting three days before the experiment. Three habituation sessions of increasing duration (20, 40, and 60 min) were run over consecutive days. During the familiarization and the recording sessions, the mouse sat inside a 3-D printed black plastic tube, leaving exposed only the head. A custom-made polyether ether ketone (PEEK) nose cone was positioned in front of the mouse, loosely fitting the mouse's snout. The nose cone was used to record the breathing signal and deliver the odorants during the experiments.

Stereotaxic probe insertion

All recordings were performed using Neuropixels 1.0 probes. The probe was mounted to a dovetail and affixed to a steel rod held by a micromanipulator (Luigs and Neumann). Before insertion, the back of the probe was coated with a solution of DiI (Thermofisher) using a paintbrush. Next, the silicone plug was removed from the craniotomies, and the probe was positioned above the recording site craniotomy (AP: 2.0/2.1 mm; ML: -2.0/-2.1 mm from bregma). Next, the probe was advanced through the dura and the cortex at approximately 5 μm/s until reaching the PCx (DV: 5.2/5.5 μm from bregma). The exact position depended on identifying a region with high firing rates and breathing-coupled activity. Then, the probe was retracted by 100 μm to allow the brain tissue to settle for 30 minutes before starting the recording. An Ag/AgCl electrode placed over the contralateral posterior parietal cortex was used for grounding. After electrode insertion, craniotomies were covered with a drop of agar solution (1% in Ringer's solution). Neuropixels data were acquired and recorded at 30 kHz through a PIXe interface board connected to a PC.

Breathing signal and other experimental signals

Four signals were acquired besides the neural data: (1) a breathing signal generated by a flow sensor (AWM3300V Honeywell) plugged into a custom-made polyether ether ketone (PEEK) nose cone was positioned in front of the mouse, loosely fitting the mouse's snout. See section *Quantification and Statistical Analyses - Analysis of the breathing signal* for a description of respiratory signal preprocessing pipeline; (2) an odor signal generated by a photo-ionization detector (200B miniPID, Aurora Scientific) that sampled the odorant inside the nose cone; (3) a TTL signaling the start of each odor trial and (4) a TTL signal generated by a Bpod Analog Input module (Sanworks) at the start of each inhalation. To identify the onset of an inhalation online, the breathing signal was fed into the Bpod Analog Input module, and a threshold was set at the breathing signal zero-crossing before the inhalation peak. All signals were digitized and recorded at 30 kHz using an Intan RHD2000 board. Finally, to align the neural data with the other signals, a 1 Hz TTL clock signal (50% duty cycle) or a barcode was generated by an Arduino One board and recorded by the PIXe board and the Intan board.

Odor delivery

Odorant stimuli were delivered using 5 seconds of odorant pulses. Odorants were delivered in 8 blocks (trials) for the two odors/three concentrations experiments, 16 blocks for the three odors/two concentrations experiments, and 10 blocks for the four odors/one concentration experiments. The order of the odorants was randomized within each block. The inter-stimulus interval was randomly drawn from an exponential distribution (mean: 40s, min-max: 30-50s).

Odorants were delivered using a custom-made Arduino-controlled 13-valve olfactometer that delivers up to 12 odorants separately. The 13th valve was used to deliver a blank stimulus (no odor) between odor presentations. A vacuum continuously exhausted lingering odors. Odorants were contained in 15 ml vials partially filled with glass beads (Sigma-Aldrich). The headspace and the volume of odorant inside the vial were chosen to ensure that the amount of odor delivered within and across trials was steady as assessed by PID measurements. Each vial was separately connected to an olfactometer valve through a 3 in.-long PTFE tubing. A custom software was used to control valve opening and closing, enabling switching between odor vials and a blank vial. At the beginning of a trial, the opening of an odor valve was synchronized with the onset of inhalation, as detected by the Bpod Analog Input Module.

Two streams of carbon-filtered air (F1 and F2) were independently routed to the nose cone at 1 l/min. The F1 stream consisted in odor (F1O; 0.1 l/min) and carrier (F1C; 0.9 l/min) streams mixed. Upon opening an odorant valve, the F1O flow was routed through the open vial to a PEEK manifold using a 3 in.-long PTFE tubing. Inside the manifold, the F1O flow from the open vial was mixed with the F1C flow to obtain the F1 airflow. The outlet of the mixing manifold was connected through a 0.5-in.-long PTFE tubing to a final three- way valve (V1). The F2 stream was directly connected to a second three-way solenoid valve (V2). The V1 and V2 valve outlets converged in a final 0.5 in. PTFE tubing connected to the nose cone. The F1 and F2 airflows reached the odor cone during odor-ON and odor-OFF epochs, respectively. The V1 outlet was open during the odor-ON epoch, whereas the V2 outlet was open during the odor-OFF epoch. At the beginning of a trial, the olfactometer opened the odor vial valve to load the tubing with odorized air up to the final valve V1, which diverted the flow outside the nose cone. After 2 seconds, the onset of an inhalation triggered an ‘‘odor-ON’’ TTL that switched the outlet opening of the V1 and V2 valves such that only the odorized airflow F1 entered the nose cone. After 5 seconds from the odor-ON TTL, the odor vial valve closed. After 10 seconds from the closing of the odorant vial valve, the V1 and V2 valves were switched to the odor-OFF configuration. The olfactometer was calibrated to generate the final odor concentration within ~200ms from the opening of the final valve. No attempt was made to remove a small pressure transient at the opening of the final valve. The odor panel included two odors (alpha-pinene and eucalyptol) delivered at three concentrations (0.01, 0.1, and 1% v./v.), three odors (limonene, p-cymene, and methyl butyrate) delivered at two concentrations (0.01 and 1% v./v.) and four odors (eugenol, dicycloexyl disulfide, p-cymene, methyl 2-furoate) delivered at a single concentration (0.01%). All odors were purchased from Sigma-Aldrich. To determine the dilution of each odor, a calibration curve was generated. To this aim, the signal generated by a photo-ionization detector (200B miniPID, Aurora) upon delivery of an odor at three dilutions (no dilution, 1:8, and 1:160 in mineral oil, Sigma-Aldrich; 10 presentations per dilution) was recorded. Then, an exponential curve was fitted to the miniPID traces to obtain the coefficient A for each dilution. Next, a second-order polynomial was fitted to the three A coefficients of each odor. Finally, the dilutions corresponding to 0.1%, 1%, and 10% v./v. of undiluted odor were extrapolated from the fitted polynomial. The carrier airflow further diluted the odor concentration by 10 to reach the final concentration of 0,01, 0.1, and 1 % v./v. (Figure 44).

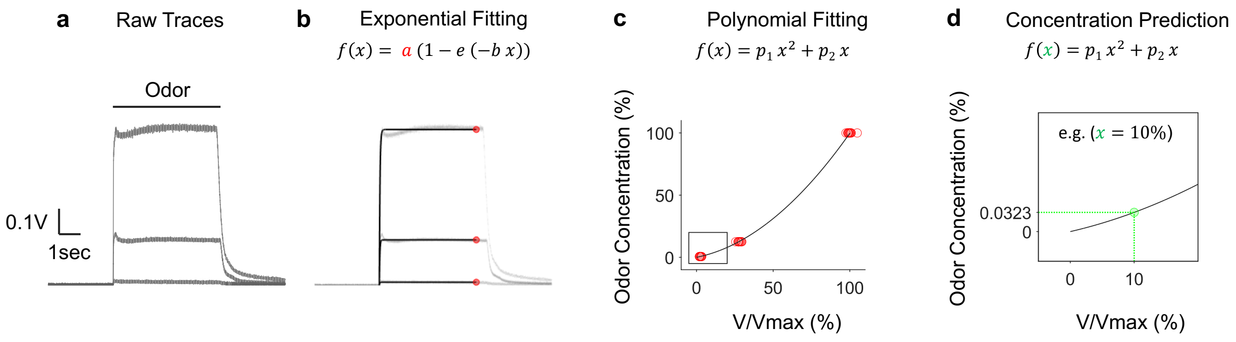

Figure 44. Pipeline for calibration of experimental odor concentrations
(**a**) Raw odor traces at the three calibration dilutions obtained from the miniPID (**b**) Exponential fitting of the raw traces (**c**) Second order polynomial fitting of the three exponential fitting coefficients (**d**) Example of a 10% concentration prediction from the fitting obtained in (c).

Artificial mechanical stimulation

The cannula in the nasopharynx was attached to a computer-controlled solenoid valve, which was connected to a vacuum line. The opening of the valve drew air inside the nasal cavity. The air was deodorized through a carbon filter before entering the nose cone. 150-ms pulses of suction at 750-ms intervals were applied. Five flow rates that span the range of estimated nasal flow rates in mice were tested (50, 100, 150, 200, and 250 ml/min).

Histology

Mice were deeply anesthetized with 1 g/kg urethane injection and intracardially perfused with 1% phosphate buffer solution (PBS) followed by 4% paraformaldehyde (PFA). The brain was dissected and immersed in 4% PFA for 24 h. Following fixation, the brain was washed with PBS and sectioned coronally (80 μm) with a vibratome. Sections were counter-stained with DAPI, and images were acquired with a fluorescence microscope at 10x magnification. The Allen CCF open-source toolbox (Shamash et al., 2018) was used to reconstruct the probe location in 3D. Briefly, sections that spanned the electrode track were first registered to the Atlas by means of multiple manually selected points that were used by the algorithm for non-rigid transformation of every section. Once registration was completed, in the transformed histology images were manually selected points representing the probe track for every anatomical section. Finally, a line was fitted on the selected probe points and rescaled on the real probe length (values collected during the recording). This procedure allowed to assign every Single Unit to a specific anatomical location in the brain. Brainrender (Claudi et al., 2021) was used to visualize the probe position.

Experimental design

No statistical methods were used to determine sample sizes. Sample sizes were chosen based on previous publications in the field. Multiple independent samples were collected for each experiment. Data collection and analyses were not performed blind to the experimental conditions. The inclusion and exclusion criteria for any data and subjects and the statistical methods are indicated in the Quantification and Statistical Analysis section.

Quantification and Statistical Analyses

Analysis of the breathing signal

The breathing signal was bandpass filtered between 0.5 to 50Hz using the MATLAB FMAToolbox (http://fmatoolbox.sourceforge.net/) and smoothed with a Gaussian kernel (standard deviation: 25ms). Inhalation peaks were identified as the local minima of the respiratory signal. Inhalation peaks closer than 65 ms from the next peak were discarded. Inhalation onset and offset were identified as the breathing signal zero-crossings before and after the inhalation peak. Inhalation length was defined as the difference between the inhalation offset and onset times. The breathing cycle was calculated as the difference between two consecutive inhalation onsets. The negative inhalation slope was defined as the slope of the line between the nearest two points before the inhalation peak in the z-scored respiration signal with a value equal to 10% and 90% of the inhalation peak amplitude. Similarly, the positive inhalation slope was calculated as the slope of the line between the 90% to 10% of inhalation amplitude points in the z-scored respiration signal after the inhalation peak.

Inhalation clustering

Inhalation waveforms were isolated by extracting the breathing signal within a 100 ms-long window centered on the inhalation peak. Each waveform was normalized by its 2-norm and considered as a point in a high-dimensional space. The dimensionality of the inhalation space was reduced by applying PCA using the ‘pca’ function in MATLAB. The projection of the inhalation vector onto the n-dimensional subspace spanned by the n first PCs (where n is the minimum number of PCs that explain at least 98% of total variance) was calculated. The inhalation vectors in the n-dimensional space were clustered with a Gaussian Mixture Model using the ‘fitgmdist’ function in MATLAB (maximum number of iterations: 10,000, regularization value: 0.05, replicates: 15, full covariance matrix). The Calinski-Harabasz index was used to determine the optimal number of clusters. The centroid vector for each cluster was defined as the mean vector of all inhalation vectors within the cluster. To consolidate the GMM clustering, a Hierarchical Cluster (HC) dendrogram was applied to the centroid vectors using the ‘linkage’ function in MATLAB (distance metric: correlation). The HC dendrogram from an individual experiment usually resulted in two or three clusters. Visual inspection of the dendrograms suggested that two clusters were similar and stemmed from the same branch; thus, the two clusters with the same parent were merged. Finally, the clusters to the ‘‘slow’’ and ‘‘fast’’ inhalation types were assigned based on the mean of the inhalation lengths within each cluster, with ‘‘fast’’ inhalation assigned to the class with smaller inhalation lengths. The clustering algorithm was cross-validated on the inhalations from eight mice by fitting the GMM on a training set consisting of all the inhalations from seven mice and then using the fitted model to predict the labels of the inhalations from the held-out mouse. The ground-truth inhalation labels for the held-out mouse were obtained using the above clustering pipeline. This process was repeated for all possible combinations of test and train sets, and the classification accuracies were finally averaged. This clustering pipeline classified the inhalation label of held-out inhalations with 98% accuracy.

Spike sorting and inclusion criteria

Spike waveforms were sorted using KiloSort3. All clusters were manually curated using Phy (https://github.com/cortex-lab/phy). The clusters were evaluated by examining their firing rate stability during the recording session, the median amplitude of the spike (>50 μV), the auto-correlograms, and the cross-correlograms. The quality of the clusters included in the analyses was further evaluated by computing the inter-spike-interval (ISI) violation rate (threshold: <0.5; median: 0.01, Q1: 0, Q3: 0.04), the amplitude cut-off (median: 0.0005, Q1: 0.0001, Q3: 0.0015), and the presence ratio (median: 1, Q1: 1, Q3: 1) (Figure 45). Single units with a firing rate of less than 0.5 Hz were excluded from the subsequent analyses; this threshold was lowered to 0.1 Hz in the experiments with tracheostomized mice because the urethane anesthesia reduced the baseline firing rate. Restricting the analyses to only those units with an ISI violation rate < 0.02 gave similar results.

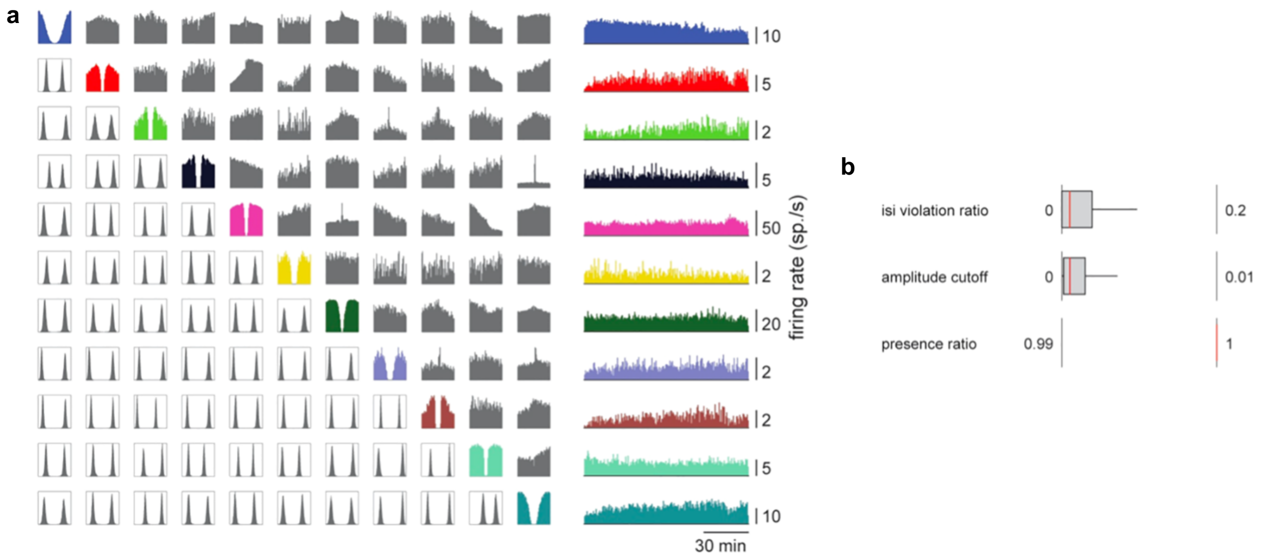

Figure 45. Metrics of single units

(**a**) auto-correlograms (main diagonal), pairwise cross-correlograms (upper matrix), and pairwise linear discriminant analyses (lower matrix) for eleven units recorded from seventeen adjacent Neuropixels 1.0 contacts in a representative recording. On the right the time-course of the firing rates for each unit. (**b**) Distribution of the ISI violation ratio, amplitude cutoff, and presence ratio for all units included in the dataset.

Single units were further classified as regular (RS) or fast-spiking (FS). A weighted average of the contributing cluster templates was computed for each unit, obtaining an average template waveform. Next, three features were extracted:

(1) The latency between the negative and the following (post-depolarization) positive peak of the average waveform;

(2) The asymmetry between the pre-depolarization (p1) and the post-depolarization (p2) peaks of the average waveform, computed as:

$$\frac{p2 - p1}{p2 + p1}$$

(3) The average firing rate of the unit across the whole recording.

Finally, a k-means clustering (with Squared Euclidean distance, 10,000 iterations, and 2,500 replicates) of the features was used to partition the units recorded from each mouse into two categories. Units labeled as ‘RS’ had, on average, lower firing rates, larger trough-to-peak latency, and smaller asymmetry compared to units labeled as ‘FS’.

The through-to-peak latency and the asymmetry index were also used to assess the homogeneity of cell-type sampling across the experimental conditions. To this aim, the distributions of the waveform features were compared across all experimental conditions (Figure 46a). Furthermore, a cross-validated Naive Bayes decoder and a linear support vector machine using these waveform features were used to ascertain that the experimental condition could not be decoded from the spike waveforms of the units recorded during that specific condition (Figure 46b).

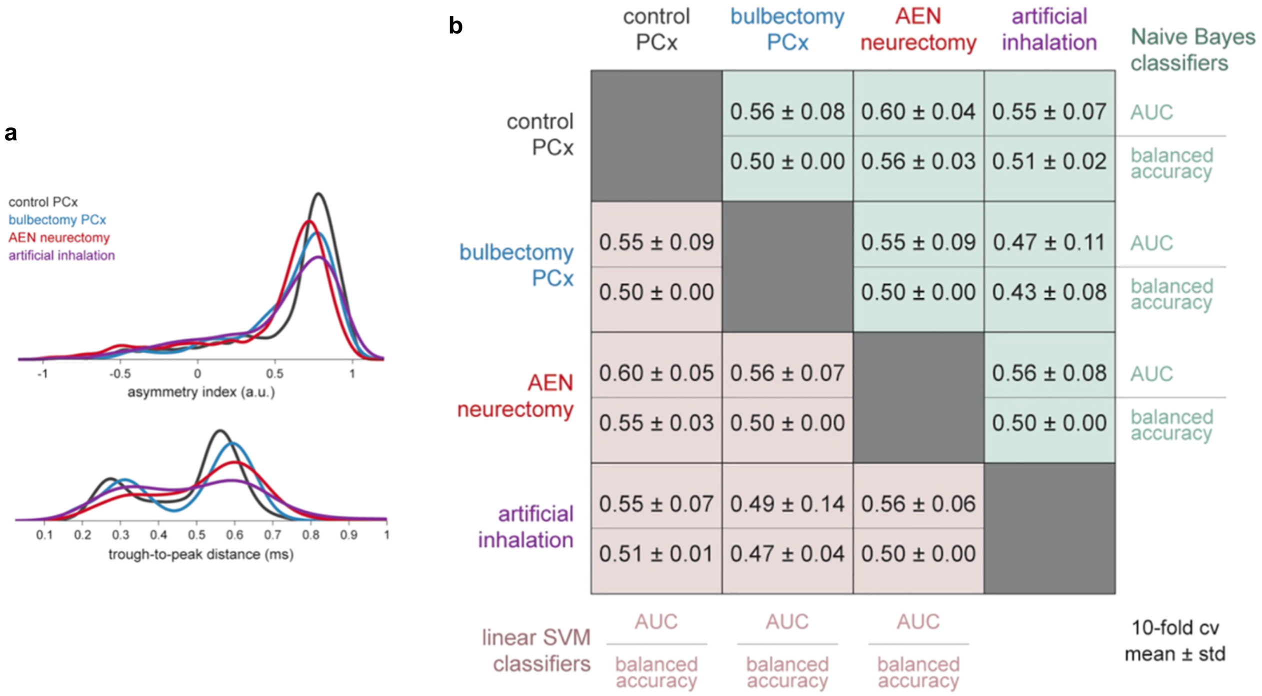

	control PCx	bulbectomy PCx	AEN neurectomy	artificial inhalation	Naive Bayes classifiers
control PCx		0.56 ± 0.08	0.60 ± 0.04	0.55 ± 0.07	AUC
		0.50 ± 0.00	0.56 ± 0.03	0.51 ± 0.02	balanced accuracy
bulbectomy PCx	0.55 ± 0.09		0.55 ± 0.09	0.47 ± 0.11	AUC
	0.50 ± 0.00		0.50 ± 0.00	0.43 ± 0.08	balanced accuracy
AEN neurectomy	0.60 ± 0.05	0.56 ± 0.07		0.56 ± 0.08	AUC
	0.55 ± 0.03	0.50 ± 0.00		0.50 ± 0.00	balanced accuracy
artificial inhalation	0.55 ± 0.07	0.49 ± 0.14	0.56 ± 0.06		
	0.51 ± 0.01	0.47 ± 0.04	0.50 ± 0.00		
linear SVM classifiers	AUC balanced accuracy	AUC balanced accuracy	AUC balanced accuracy		10-fold cv mean ± std

Figure 46. Waveforms comparison across experimental conditions

(**a**) Distributions of two spike waveform features for each experimental condition. Top: asymmetry index; bottom: through-to-peak latency. (**b**) Decoding the experimental condition based on the spike waveform features of the units recorded in each condition. Upper matrix: AUC and accuracy using a cross-validated Naïve Bayes classifier for each pair of experimental conditions. Lower matrix: AUC and accuracy using a cross-validated linear support vector machine for each pair of experimental conditions. Mean ± standard deviation is indicated.

‘

Analysis of sniff-by-sniff responses

Inhalation and odor response were measured as the average spike count within a 70ms or 180ms window after the inhalation onset. Smoothed peri-event time histograms (PETH) were obtained by convolving the spike-times series within an inhalation with a Gaussian kernel (standard deviation: 10ms), then averaging across all inhalations of the same type and finally subtracting the average firing rate across the odor-free epochs of the entire recording session. PETHs were aligned at the inhalation onset. Odorless-air inhalations were defined as those occurring within the -13s to -4s window before the delivery of an odor. This window was considered sufficient to remove any lingering odor because the minimum time interval between two odor presentations was 30 seconds, and a vacuum line constantly exhausted odorants from the nose mask. Sniff-by-sniff odor responses were measured in a time window starting at the odor onset and lasting for 5 seconds. The first two trials of each odor-concentration stimulus were excluded to avoid any bias due to the novelty of the stimulus.

To ascertain whether a neuron responded to an inhalation, the spikes within a window comprising the inhalation onset (from -300ms to +400ms) were binned using an adaptive binning method, guaranteeing at least five spikes per bin. Then, the spike counts in those bins were compared against those generated by a homogenous Poisson process using a chi-square test. The constant rate of the homogenous Poisson process was set to the mean firing rate of the recorded neuron. Responses to first sniffs were tested by comparing the spike counts in a 180ms window post-inhalation onset in the first sniff after at least five consecutive slow inhalations against the spike counts in a 180ms window post-inhalation onset in the remaining slow inhalations. For all these analyses, only odorless inhalations were considered.

Concentration discrimination index

To measure how well a neuron could discriminate two concentrations, first was computed computed an area-under-the-receiver-operating-curve (auROC) using the spike counts during the inhalation of 0.01 and 0.1% v./v. odorant. The CDI was computed as abs(1 - 2*auROC). To generate the spike count distribution for each concentration, a random sample of inhalations was taken during the presentation of that concentration; an equal sample size was used for the two concentrations. Next, three different CDI were calculated based on a sample of slow inhalations, fast inhalations, and mixed slow and fast inhalations; 100 samples were drawn for each set of inhalations, and an average CDI was calculated for slow, fast, and mixed inhalations.

Tuning curves

To obtain neural tuning curves during artificial stimulation of the nasal cavity, the average response for each airflow rate was calculated as the difference between the number of spikes fired by a neuron during the (0 500] and (-500 0] ms window where 0 is the onset of the air pulse. To obtain neural tuning curves during natural breathing, inhalations were sorted into ten quantile bins based on the amplitude of the peak of airflow as measured by the flow sensor. This was done to ensure that each bin contained an equal number of inhalations. The tuning curve was generated by using the average response to an odorless inhalation during the first 180ms for each bin. Tuning curves were z-scored, and their slopes were calculated by linearly regressing the neural response to the airflow rate.

Encoding models

A Poisson Generalized linear model (GLM) with regularization was employed to estimate the contribution of inhalation speed, odor concentration, and their interaction with the sniff-by-sniff odor response of a neuron. The model aimed to predict the spike count (γ_i) of neuron i during a single inhalation (either first 180 ms or 70 ms) using the following equation:

$$\gamma_i \sim Poiss\ (\exp(\alpha_i I + \beta_i C + \gamma_i IC + \gamma_{0i}))$$

Here, the I term represents the inhalation speed (0 for slow and 1 for fast), and the C term represents the odor concentration (logarithm of the three concentrations 0.01, 0.1 and 1% v./v.). γ_{0i} is a baseline bias of the response. The GLM was fitted using the glmnet toolbox (https://hastie.su.domains/glmnet_matlab/) in MATLAB with elastic net regularization, where the parameter alpha controlled elastic net penalty. A value of 0.95 was used for *alpha*, which smoothly interpolates the gap between lasso (*alpha* = 0) and ridge regression (*alpha* = 1). The optimal elastic net penalty value was selected using a 10-fold cross-validation approach. A linear regression model was used for the simulations shown in Figure 36, Figure 37, Figure 39 and Figure 40. In this case, the normalized firing rate r_i of neuron i during the first 180 ms of inhalation was modeled with the following equation:

$$z\,score\,(r_i) = \alpha_i I + \beta_i C + r_{0i} + \eta$$

Here, the I term represents the inhalation speed (0 for slow and 1 for fast), and the C term represents the odor concentration (varying from 0 to 1 based on the logarithm of the concentration). The term r_0 is a baseline bias, and η is a Gaussian noise term. To fit the models, inhalations were randomly sampled from all inhalations to have an equal size for each combination of inhalation speed and odor concentration term. The vector of the neural responses to the inhalations was z-scored and passed to the model with the corresponding design matrix. The significance of the model's coefficients was assessed using an ANOVA test. The random sampling was repeated 100 times, and the coefficients of each term and their p-values were averaged across all re-samplings.

PCA embeddings

To visualize the neural representation of odor concentrations across different inhalation speeds, PCA analysis was performed on the response covariance matrices obtained from a neural pseudo-population or single mouse neural populations. Before applying PCA, the neural responses of individual neurons were z-scored. PCA was also used to determine the projections onto the first 15 PCs of the sniff-by-sniff responses; these projections were separately used to decode inhalation speed and odor concentration in Figure 34 and Figure 35.

Angle between encoding axes

The encoding direction for odor concentrations and inhalation speed was determined using concentration-encoding unit vectors and sampling-encoding unit vectors; these two vectors were defined as unit vectors in the sniff-by-sniff response space. Linear discriminant analysis (LDA) was used to calculate the encoding vectors. Specifically, a pseudo-population response matrix with corresponding labels for each odor concentration and inhalation speed was used to fit the LDA model. This operation was performed using the *Python scikit-learn* library (Pedregosa et al., 2011). The eigenvalue decomposition solver was used to fit the LDA model with a shrinkage parameter that was automatically calculated by the Ledoit-Wolf lemma algorithm. The encoding vector was taken as the first column of the LDA transform scaling matrix. For each inhalation speed, the concentration-encoding unit vector was obtained from the LDA fit by using a pseudo-population response during a given inhalation speed and concentration using a different label for each concentration. Similarly, the inhalation-encoding unit vector was obtained from the LDA fit using pseudo-population response during either inhalation speed, and the type of inhalation speed was used as a label. Finally, the average angle between the concentration-encoding vectors for each inhalation speed and the average angle Θ between the concentration-encoding vectors and inhalation-encoding vectors were calculated and then transformed as: $\Theta' = 90 - |90 - \Theta|$. This procedure was repeated 100 times with pseudo-population response matrices built using different randomly sampled neurons for each run.

Inhalation speed decoding

A linear support vector machine (lSVM) classifier was utilized for all classification analyses (inhalation speed, odor concentration, odor identity, and generalization analysis). The lSVM was implemented using the MATLAB Neural Decoding Toolbox (NDT) (Meyers, 2013) and *libsvm* (http://www.csie.ntu.edu.tw/%7Ecjlin/libsvm/) toolbox. A 10-fold cross-validation was performed for all models. Before model fitting, the sniff-by-sniff neural responses in the training and test set were normalized by subtracting the means and standard deviations calculated from the responses in the training set.

To decode the inhalation speed, a pseudo-population response matrix was generated using only the spike counts during 180ms windows for each inhalation of odorless air. Specifically, 400 random slow and fast inhalations were drawn, and the spike counts in 180ms windows were used to build the response matrix of a pseudo-population or an individual mouse population. The decoding accuracy for different numbers of neurons was determined by drawing random subsamples of neurons of different numerosity. This resampling process was repeated 100 times for each number of neurons to obtain reliable estimates of decoding accuracy. Additionally, the entire classification process was repeated 100 times, randomizing the sampled inhalation events included in each run. The reported accuracy for each number of neurons represents the mean of all resampling processes.

Inhalation phase decoding

To predict the inhalation phase from neuronal activity, we employed Support Vector Regression (SVR) using the scikit-learn library (Pedregosa et al., 2011).

Preprocessing

First, the firing rate for every neuron was computed using a rolling gaussian window with sd = 20ms (gaussian_filter() from scipy.nd-image). The firing rate matrix and the respiration trace were then downsampled to 10ms bins to speed up the following computations. For every animal, the analysis was restricted to areas with at least 20 recorded neurons.

Inhalation phase

Analysis was restricted to the inhalation events defined and classified as described in the section *Inhalation clustering*. The inhalation phase was a number in the interval [0, 1] where 0 and 1 corresponded to the beginning and the end of the inhalation event, and the other values were linearly interpolated.

PCA decomposition

First, neuronal activity from all the neurons of each area was projected over principal components using the PCA class from sklearn. decomposition. To focus on the most relevant components for the prediction, PCs up to a cumulative explained (relative) variance > 0.5 were included (at least two PCs were always selected). We note that the analysis results hold for different inclusion criteria for the number of PCs.

Epochs definition

For the training and testing of the model, suitable non-overlapping epochs were created by concatenating inhalation periods for a total duration of 30s. Depending on the inhalation number and classification, this resulted in a variable number of epochs (between 2 and 4) for every experimental animal. For every animal, all permutations of pairs of those suitable epochs were used as test and training datasets. Results were robust to different choices of epochs (i.e., more epochs with shorter windows).

SVR training

An SVR model was trained using SVR from sklearn.svm(), and its default parameters (kernel = ’rbf’, degree = 3, gamma = ’scale’, coef0 = 0.0, tol = 0.001, C = 1.0, epsilon = 0.1, shrinking = True; where ’rbf’ kernel is the Radial Basis Function, and ’scale’ gamma is 1 / (n_features * X.var())). The source data was the (n_components, timepoints) array of PC data; the variable to predict was the (timepoints,) array of inhalation phase data. The shuffle distributions were calculated by randomizing the inhalation phase array before prediction.

Evaluation

For every permutation of the epochs, the inhalation phase was predicted at every time point, and the performance of the model was assessed by calculating the squared Pearson correlation between the ground truth and the predicted data and then averaged across permutations.

Concentration decoding

To classify odor concentration (0.01, 0.1, and 1% v./v.), a pseudo-population response matrix or a single animal population response matrix was built using the same number of inhalations for each odor-concentration pair to avoid any potential bias due to different inhalation sample sizes. Next, for each odor, corresponding rows of this matrix or its PC projections were sorted and passed to the classifier to decode the concentration in either the whole population response space or its PC projections space. This procedure was repeated 100 times with pseudo-population response matrices with different randomly sampled inhalations. The reported accuracies are the mean and standard deviation across all resampling processes. To investigate the geometry of the neural space, a generalization paradigm was employed. To this end, a lSVM trained on data from one inhalation speed was tested on data from the other inhalation speed (*trans*-decoder). The average accuracy of *trans*-decoders was compared to that of *cis*-decoders that had been trained and tested instead on the odor responses during the same inhalation speed. To assess the importance of heterogeneous selectivity for mechanosensory and olfactory inputs for sniff-invariant odor representations, the sniff-by-sniff responses of individual neurons was fit with a linear regression model including a concentration (C = 0.01, 0.1, and 1%) and an inhalation speed (slow: I = 0; fast: I = 1) regressor. Then we selected a sub-pseudo-population with highly correlated mechanosensory (α) and olfactory regressor coefficients (β). To this end, a sub-pseudo-population of neurons meeting the following conditions were considered positively correlated: $(|\beta| \geq |\alpha * \tan\left(\frac{\pi}{12}\right)|)$ and $(|\beta| \leq |\alpha * \tan\left(5 * \frac{\pi}{12}\right)|)$ with α and β having the same sign. Finally, another subset of neurons with α and β having different signs was selected to build a sub-pseudo-population with negatively correlated mechanosensory and concentration regressors. The union of these two sets was considered as the uncorrelated sub-pseudo-population. Then, an equal number of neurons was randomly sampled from these three sub-pseudo-populations, and their sniff-by-sniff odor responses were used by cis- and trans-decoders. To decode odor concentration over time and phase bins, we used the following procedure:

Feature vectors generation

First, we generated time- and phase-binned vectors of neuronal activity after the inhalation onset as follows:

(1) Time-binned vectors of 180ms: the firing rate traces of all neurons in an area were used, as defined in the above section *Inhalation phase decoding – Preprocessing*. The traces were cropped from the onset of each inhalation in a 180ms window and binned in 10-ms bins. Then, the traces of all neurons were concatenated to obtain, for every inhalation, an array with size (n_timebins x n_neurons), with n_timebins = 18.

(2) One-bin time vectors: the time-binned arrays defined above were averaged over the time bins.

(3) Time-binned vectors cropped over a full inhalation cycle: the respiratory phase was computed using the Hilbert transform. The time window in which the respiratory phase

increased by 2π was found for every inhalation. Then, the firing rate trace was cropped in this window, padding it with zeros to account for the different durations of each inhalation period to a total of 500ms (enough to accommodate > 99% of all inhalations). The arrays were then binned in 10-ms bins and concatenated across neurons to a total of (n_timebins x n_neurons) for every inhalation, with n_timebins = 50.

(4) Phase-binned vectors: the respiratory phase was computed using the Hilbert transform. The time window in which the respiratory phase increased by 2π was found for every inhalation. The firing rate trace was cropped in this window and then binned into 36 bins equally spaced in phase (in this case, no zero-padding was necessary). Next, the activity of all neurons was concatenated to obtain an array with length (n_phasebins x n_neurons) for every inhalation, with n_phasebins = 36 and zero-padding at the end to ensure array length consistency.

Odor concentration decoding

To decode odor concentration from the firing rates, we used an SVM classifier using a generalization procedure like the one described above. First, inhalations were sampled 100 times with replacement for every animal to obtain a consistent number of events for each combination (inhalation_type, concentration). Then, ten-fold validation was used for training and testing the classifier for each extraction. Data were split into ten blocks, and the SVM trained over nine blocks and tested over the remaining one iterating over all ten possible left-out blocks. The SVM model was trained using SVC from sklearn.svm, and its default parameters but for the linearity of the kernel (kernel = linear, gamma = ’scale’, coef0 = 0.0, tol = 0.001, C = 1.0, epsilon = 0.1, shrinking = True; where ’scale’ gamma is 1/(n_features * X.var())). The source data was the ((n_bins x n_neurons), n_inhalations) array of concatenated firing rates over time for each inhalation; the variable to predict was the (n_inhalations) array of concentrations presented during each inhalation. For each iteration, the SVM was evaluated by computing the fraction of correct predictions. This number was then averaged across all folds and samplings (1000 different classifications) to obtain the numbers reported in the figures. Finally, the analysis was repeated separately for the two presented odors, and the results eventually merged.

Simulation of sniff-induced concentration changes

We tested whether integrating odor-independent mechanosensory inputs in the piriform cortex code offsets the odor concentration alteration (ΔIC) inside the nasal cavity due to changes in inhalation speed. To this end, we compared odor concentration decoding using the activity pattern of two simulated populations of neurons with or without mechanosensory inputs. We reasoned that the ΔIC should be proportional to the external concentration and additive. Thus, we simulated the sniff-by-sniff responses of each neuron using the following Poisson model:

$$R_j = \ Poiss\left(\alpha_j I + \ \beta_j C_n\right) \text{ with } C_n = \log\left(C_e + k\, I\, C_e\right)$$

R_j is the simulated neural response during a sniff. α_j and β_j are the mechanosensory and olfactory regressor coefficients previously estimated using a linear regression model fitted to the actual responses of neuron j. I is equal to 0 for slow inhalations and 1 for fast inhalations. C_e is the external odor concentration (0.01, 0.1, and 1%). k is a proportional factor that was parametrically changed in the range between 0 and 1 to simulate different levels of ΔIC; k = 0 means that a slow-to-fast change in inhalation speed does not change the odorant concentration (ΔIC = 0), whereas k = 1 means that a slow-to-fast change in inhalation speed increases the odor concentration inside the naris by 100% of the external concentration (ΔIC = C_e). The population of neurons without mechanosensory inputs was generated by setting α to 0. α was set to 0 to simulate the population of neurons without mechanosensory inputs.

Geometrical proof

Heterogeneous mixed selectivity of neural responses has an immediate connection with the orthogonality of population representations. This can be seen in a simple model, as follows. Consider a population code where the firing rate r_i of cell i is

$$r_i = \ r_0 + \alpha_i I + \ \beta_i C + \ \gamma_i IC$$

where, as above, *I* is the inhalation speed, and *C* is the concentration. For a population of size N ($1 \leq i \leq N$), we can also write this in vector form as

$$r = r + \alpha I + \beta C + \gamma I C$$

where r, α, β and γ are now vectors with N entries. Assume that the number N of neurons is large and that coding is heterogeneous (that is, there is no special structure to the code), so that α, β and γ are random vectors in N dimensions. In this case, α can be thought of as a scalar $|\alpha|$ controlling the overall intensity of tuning for inhalation speed in the population, times a random vector on the unit sphere, and the same for β and γ. The direction along which the population vector r encodes the concentration is

$$\frac{dr}{dC} = \beta + \gamma I$$

In other words, the concentration C is encoded in the direction β for slow inhalation (I=0) and the direction $\beta + \gamma$ for fast inhalation (I=1). The cosine of the angle θ between the two encoding directions is

$$\cos(\theta) = \frac{< \beta, \beta + \gamma >}{|\beta| \cdot |\beta + \gamma|} = \frac{|\beta|^2 + < \beta, \gamma >}{|\beta| \sqrt{|\beta|^2 + |\gamma|^2 + 2 < \beta, \gamma >}}$$

However, if β and γ are high-dimensional and their direction is chosen at random, it can be assumed they are approximately orthogonal, and $< \beta, \gamma > \approx 0$. Accordingly,

$$\cos(\theta) \approx \frac{|\beta|^2}{|\beta| \sqrt{|\beta|^2 + |\gamma|^2}} = \frac{|\beta|}{\sqrt{|\beta|^2 + |\gamma|^2}}$$

Therefore, the concentration encoding directions will tend towards orthogonality in the presence of strong interactions (when $\gamma \gg \beta, \cos(\theta) = 0$) and will be parallel when interactions are absent or weak (when $|\gamma| = 0, \cos(\theta) = 1$).

Statistical tests

Sample sizes were not estimated in advance. Data groups were tested for normality using Kolmogorov-Smirnov test and then compared using the appropriate test. For regression modeling, confidence intervals were computed over bootstraps (with replacement) of the data. Statistical tests used, the value of n, and what n represents in each analysis can be found in the corresponding figure legend.

Bibliography

Adrian, E.D., 1942. Olfactory reactions in the brain of the hedgehog. The Journal of Physiology 100, 459–473. https://doi.org/10.1113/jphysiol.1942.sp003955

Arzi, A., Rozenkrantz, L., Gorodisky, L., Rozenkrantz, D., Holtzman, Y., Ravia, A., Bekinschtein, T.A., Galperin, T., Krimchansky, B.-Z., Cohen, G., Oksamitni, A., Aidinoff, E., Sacher, Y., Sobel, N., 2020. Olfactory sniffing signals consciousness in unresponsive patients with brain injuries. Nature 581, 428–433. https://doi.org/10.1038/s41586-020-2245-5

Ashhad, S., Kam, K., Del Negro, C.A., Feldman, J.L., 2022. Breathing Rhythm and Pattern and Their Influence on Emotion. Annu. Rev. Neurosci. 45, 223–247. https://doi.org/10.1146/annurev-neuro-090121-014424

Attinger, A., Wang, B., Keller, G.B., 2017. Visuomotor Coupling Shapes the Functional Development of Mouse Visual Cortex. Cell 169, 1291-1302.e14. https://doi.org/10.1016/j.cell.2017.05.023

Bocca, E., Antonelli, A.R., Mosciaro, O., 1965. Mechanical Co-Factors in Olfactory Stimulation. Acta Oto-Laryngologica 59, 243–247. https://doi.org/10.3109/00016486509124558

Bolding, K.A., Franks, K.M., 2018. Recurrent cortical circuits implement concentration-invariant odor coding 14.

Bolding, K.A., Franks, K.M., 2017. Complementary codes for odor identity and intensity in olfactory cortex. eLife 6, e22630. https://doi.org/10.7554/eLife.22630

Bolding, K.A., Nagappan, S., Han, B.-X., Wang, F., Franks, K.M., 2020. Recurrent circuitry is required to stabilize piriform cortex odor representations across brain states. eLife 9, e53125. https://doi.org/10.7554/eLife.53125

Catania, K.C., 2013. Stereo and serial sniffing guide navigation to an odour source in a mammal. Nat Commun 4, 1441. https://doi.org/10.1038/ncomms2444

Chang, R.B., Strochlic, D.E., Williams, E.K., Umans, B.D., Liberles, S.D., 2015. Vagal Sensory Neuron Subtypes that Differentially Control Breathing. Cell 161, 622–633. https://doi.org/10.1016/j.cell.2015.03.022

Chong, E., Moroni, M., Wilson, C., Shoham, S., Panzeri, S., Rinberg, D., 2020. Manipulating synthetic optogenetic odors reveals the coding logic of olfactory perception. Science 368, eaba2357. https://doi.org/10.1126/science.aba2357

Claudi, F., Tyson, A.L., Petrucco, L., Margrie, T.W., Portugues, R., Branco, T., 2021. Visualizing anatomically registered data with brainrender. eLife 10, e65751. https://doi.org/10.7554/eLife.65751

Connelly, T., Yu, Y., Grosmaitre, X., Wang, J., Santarelli, L.C., Savigner, A., Qiao, X., Wang, Z., Storm, D.R., Ma, M., 2015. G protein-coupled odorant receptors underlie mechanosensitivity in mammalian olfactory sensory neurons. Proc. Natl. Acad. Sci. U.S.A. 112, 590–595. https://doi.org/10.1073/pnas.1418515112

Crapse, T.B., Sommer, M.A., 2008. Corollary discharge across the animal kingdom. Nat Rev Neurosci 9, 587–600. https://doi.org/10.1038/nrn2457

Crimaldi, J., Lei, H., Schaefer, A., Schmuker, M., Smith, B.H., True, A.C., Verhagen, J.V., Victor, J.D., 2022. Active sensing in a dynamic olfactory world. J Comput Neurosci 50, 1–6. https://doi.org/10.1007/s10827-021-00798-1

Del Negro, C.A., Funk, G.D., Feldman, J.L., 2018. Breathing matters. Nat Rev Neurosci 19, 351–367. https://doi.org/10.1038/s41583-018-0003-6

Eiting, T., Wachowiak, M., 2018. Artificial Inhalation Protocol in Adult Mice. BIO-PROTOCOL 8. https://doi.org/10.21769/BioProtoc.3024

Esquivelzeta Rabell, J., Mutlu, K., Noutel, J., Martin Del Olmo, P., Haesler, S., 2017. Spontaneous Rapid Odor Source Localization Behavior Requires Interhemispheric Communication. Current Biology 27, 1542-1548.e4. https://doi.org/10.1016/j.cub.2017.04.027

Findley, T.M., Wyrick, D.G., Cramer, J.L., Brown, M.A., Holcomb, B., Attey, R., Yeh, D., Monasevitch, E., Nouboussi, N., Cullen, I., Songco, J.O., King, J.F., Ahmadian, Y., Smear, M.C., 2021. Sniff-synchronized, gradient-guided olfactory search by freely moving mice. eLife 10, e58523. https://doi.org/10.7554/eLife.58523

Fontanini, A., Spano, P., Bower, J.M., 2003. Ketamine–Xylazine-Induced Slow (1.5 Hz) Oscillations in the Rat Piriform (Olfactory) Cortex Are Functionally Correlated with Respiration. J. Neurosci 23, 7993–8001.

Fulton, K.A., Zimmerman, D., Samuel, A., Vogt, K., Datta, S.R., 2024. Common principles for odour coding across vertebrates and invertebrates. Nat. Rev. Neurosci. 25, 453–472. https://doi.org/10.1038/s41583-024-00822-0

Gire, D.H., Kapoor, V., Arrighi-Allisan, A., Seminara, A., Murthy, V.N., 2016. Mice Develop Efficient Strategies for Foraging and Navigation Using Complex Natural Stimuli. Current Biology 26, 1261–1273. https://doi.org/10.1016/j.cub.2016.03.040

Grosmaitre, X., Santarelli, L.C., Tan, J., Luo, M., Ma, M., 2007. Dual functions of mammalian olfactory sensory neurons as odor detectors and mechanical sensors. Nat Neurosci 10, 348–354. https://doi.org/10.1038/nn1856

Huston, S.J., Stopfer, M., Cassenaer, S., Aldworth, Z.N., Laurent, G., 2015. Neural Encoding of Odors during Active Sampling and in Turbulent Plumes. Neuron 88, 403–418. https://doi.org/10.1016/j.neuron.2015.09.007

Idrees, S., Baumann, M.P., Franke, F., Münch, T.A., Hafed, Z.M., 2020. Perceptual saccadic suppression starts in the retina. Nat Commun 11, 1977. https://doi.org/10.1038/s41467-020-15890-w
Iwata, R., Kiyonari, H., Imai, T., 2017. Mechanosensory-Based Phase Coding of Odor Identity in the Olfactory Bulb. Neuron 96, 1139-1152.e7. https://doi.org/10.1016/j.neuron.2017.11.008

Johnson, B.N., Mainland, J.D., Sobel, N., 2003. Rapid Olfactory Processing Implicates Subcortical Control of an Olfactomotor System. Journal of Neurophysiology 90, 1084–1094. https://doi.org/10.1152/jn.00115.2003

Jordan, R., Fukunaga, I., Kollo, M., Schaefer, A.T., 2018a. Active Sampling State Dynamically Enhances Olfactory Bulb Odor Representation. Neuron 98, 1214-1228.e5. https://doi.org/10.1016/j.neuron.2018.05.016

Jordan, R., Kollo, M., Schaefer, A.T., 2018b. Sniffing Fast: Paradoxical Effects on Odor Concentration Discrimination at the Levels of Olfactory Bulb Output and Behavior. eNeuro 5, ENEURO.0148-18.2018. https://doi.org/10.1523/ENEURO.0148-18.2018

Kaupp, U.B., 2010. Olfactory signalling in vertebrates and insects: differences and commonalities. Nat Rev Neurosci 11, 188–200. https://doi.org/10.1038/nrn2789

Kepecs, A., Uchida, N., Mainen, Z.F., 2006. The Sniff as a Unit of Olfactory Processing. Chemical Senses 31, 167–179. https://doi.org/10.1093/chemse/bjj016

Khan, A.G., Sarangi, M., Bhalla, U.S., 2012. Rats track odour trails accurately using a multi-layered strategy with near-optimal sampling. Nat Commun 3, 703. https://doi.org/10.1038/ncomms1712

Kvitsiani, D., Ranade, S., Hangya, B., Taniguchi, H., Huang, J.Z., Kepecs, A., 2013. Distinct behavioural and network correlates of two interneuron types in prefrontal cortex. Nature 498, 363–366. https://doi.org/10.1038/nature12176

Lutz, A., Greischar, L.L., Rawlings, N.B., Ricard, M., Davidson, R.J., 2004. Long-term meditators self-induce high-amplitude gamma synchrony during mental practice. Proc. Natl. Acad. Sci. U.S.A. 101, 16369–16373. https://doi.org/10.1073/pnas.0407401101

Mainland, J., Sobel, N., 2006. The Sniff Is Part of the Olfactory Percept. Chemical Senses 31, 181–196. https://doi.org/10.1093/chemse/bjj012

Mainland, J.D., Lundström, J.N., Reisert, J., Lowe, G., 2014. From molecule to mind: an integrative perspective on odor intensity. Trends in Neurosciences 37, 443–454. https://doi.org/10.1016/j.tins.2014.05.005

Maurer, M., Papotto, N., Sertel-Nakajima, J., Schueler, M., De Col, R., Möhrlen, F., Messlinger, K., Frings, S., Carr, R.W., 2019. Photoactivation of olfactory sensory neurons does not affect action potential conduction in individual trigeminal sensory axons innervating the rodent nasal cavity. PLoS ONE 14, e0211175. https://doi.org/10.1371/journal.pone.0211175

Meyers, E.M., 2013. The neural decoding toolbox. Front. Neuroinform. 7. https://doi.org/10.3389/fninf.2013.00008

Miura, S.K., Scanziani, M., 2022. Distinguishing externally from saccade-induced motion in visual cortex. Nature 610, 135–142. https://doi.org/10.1038/s41586-022-05196-w

Moberly, A.H., Schreck, M., Bhattarai, J.P., Zweifel, L.S., Luo, W., Ma, M., 2018. Olfactory inputs modulate respiration-related rhythmic activity in the prefrontal cortex and freezing behavior. Nat Commun 9, 1528. https://doi.org/10.1038/s41467-018-03988-1

Pashkovski, S.L., Iurilli, G., Brann, D., Chicharro, D., Drummey, K., Franks, K., Panzeri, S., Datta, S.R., 2020. Structure and flexibility in cortical representations of odour space. Nature. https://doi.org/10.1038/s41586-020-2451-1

Pedregosa, F., Varoquaux, G., Gramfort, A., Michel, V., Thirion, B., Grisel, O., Blondel, M., Prettenhofer, P., Weiss, R., Dubourg, V., Vanderplas, J., Passos, A., Cournapeau, D., 2011. Scikit-learn: Machine Learning in Python. MACHINE LEARNING IN PYTHON J. Mach. Learn.

Perl, O., Ravia, A., Rubinson, M., Eisen, A., Soroka, T., Mor, N., Secundo, L., Sobel, N., 2019. Human non-olfactory cognition phase-locked with inhalation. Nat Hum Behav 3, 501–512. https://doi.org/10.1038/s41562-019-0556-z

Reddy, G., Murthy, V.N., Vergassola, M., 2022. Olfactory Sensing and Navigation in Turbulent Environments. Annu. Rev. Condens. Matter Phys. 13, 191–213. https://doi.org/10.1146/annurev-conmatphys-031720-032754

Roberts, B.L., Russell, I.J., 1972. The activity of the lateral-line efferent neurones in stationary and swimming dogfish. J. Exp. Biol. 435–448.

Rygg, A.D., Van Valkenburgh, B., Craven, B.A., 2017. The Influence of Sniffing on Airflow and Odorant Deposition in the Canine Nasal Cavity. Chemical Senses 42, 683–698. https://doi.org/10.1093/chemse/bjx053

Schoonover, C.E., Ohashi, S.N., Axel, R., Fink, A.J.P., 2021. Representational drift in primary olfactory cortex. Nature 594, 541–546. https://doi.org/10.1038/s41586-021-03628-7

Shamash, P., Carandini, M., Harris, K.D., Steinmetz, N.A., 2018. A tool for analyzing electrode tracks from slice histology. https://doi.org/10.1101/447995

Shusterman, R., Sirotin, Y.B., Smear, M.C., Ahmadian, Y., Rinberg, D., 2018. Sniff Invariant Odor Coding. eNeuro 5, ENEURO.0149-18.2018. https://doi.org/10.1523/ENEURO.0149-18.2018

Shusterman, R., Smear, M.C., Koulakov, A.A., Rinberg, D., 2011. Precise olfactory responses tile the sniff cycle. Nat Neurosci 14, 1039–1044. https://doi.org/10.1038/nn.2877

Smear, M., Shusterman, R., O'Connor, R., Bozza, T., Rinberg, D., 2011. Perception of sniff phase in mouse olfaction. Nature 479, 397–400. https://doi.org/10.1038/nature10521

Sobel, N., Prabhakaran, V., Desmond, J.E., Glover, G.H., Goode, R.L., Sullivan, E.V., Gabrieli, J.D.E., 1998. Sniffing and smelling: separate subsystems in the human olfactory cortex. Nature 392, 282–286. https://doi.org/10.1038/32654

Spors, H., Grinvald, A., 2002. Spatio-Temporal Dynamics of Odor Representations in the Mammalian Olfactory Bulb. Neuron 34, 301–315. https://doi.org/10.1016/S0896-6273(02)00644-X

Steele, T.J., Lanz, A.J., Nagel, K.I., 2023. Olfactory navigation in arthropods. J Comp Physiol A 209, 467–488. https://doi.org/10.1007/s00359-022-01611-9

Stettler, D.D., Axel, R., 2009. Representations of Odor in the Piriform Cortex. Neuron 63, 854–864. https://doi.org/10.1016/j.neuron.2009.09.005

Stringer, C., Pachitariu, M., Steinmetz, N., Reddy, C.B., Carandini, M., Harris, K.D., 2019. Spontaneous behaviors drive multidimensional, brainwide activity. Science 364, eaav7893. https://doi.org/10.1126/science.aav7893

Subramanian, D., Alers, A., Sommer, M.A., 2019. Corollary Discharge for Action and Cognition. Biological Psychiatry: Cognitive Neuroscience and Neuroimaging 4, 782–790. https://doi.org/10.1016/j.bpsc.2019.05.010

Tantirigama, M.L.S., Zolnik, T., Judkewitz, B., Larkum, M.E., Sachdev, R.N.S., 2020. Perspective on the Multiple Pathways to Changing Brain States. Front. Syst. Neurosci. 14, 23. https://doi.org/10.3389/fnsys.2020.00023

Teghtsoonian, R., Teghtsoonian, M., 1978. Invariance of Odor Strength with Sniff Vigor: An Olfactory Analogue to Size Constancy. J. Exp. Psychol. Hum. Percept. Perform. 4, 144–152. https://doi.org/10.1037//0096-1523.4.1.144

Tort, A.B.L., Brankačk, J., Draguhn, A., 2018. Respiration-Entrained Brain Rhythms Are Global but Often Overlooked. Trends in Neurosciences 41, 186–197. https://doi.org/10.1016/j.tins.2018.01.007
Uchida, N., Mainen, Z.F., 2003. Speed and accuracy of olfactory discrimination in the rat. Nat Neurosci 6, 1224–1229. https://doi.org/10.1038/nn1142

Wachowiak, M., 2011. All in a Sniff: Olfaction as a Model for Active Sensing. Neuron 71, 962–973. https://doi.org/10.1016/j.neuron.2011.08.030

Wallach, A., Sawtell, N.B., 2023. An internal model for canceling self-generated sensory input in freely behaving electric fish. Neuron 111, 2570-2582.e5. https://doi.org/10.1016/j.neuron.2023.05.019

Wesson, D.W., Carey, R.M., Verhagen, J.V., Wachowiak, M., 2008. Rapid Encoding and Perception of Novel Odors in the Rat. PLoS Biol 6, e82. https://doi.org/10.1371/journal.pbio.0060082

Wilson, C.D., Serrano, G.O., Koulakov, A.A., Rinberg, D., 2017. A primacy code for odor identity. Nat Commun 8, 1477. https://doi.org/10.1038/s41467-017-01432-4

Zelano, C., Jiang, H., Zhou, G., Arora, N., Schuele, S., Rosenow, J., Gottfried, J.A., 2016. Nasal Respiration Entrains Human Limbic Oscillations and Modulates Cognitive Function. J. Neurosci. 36, 12448–12467. https://doi.org/10.1523/JNEUROSCI.2586-16.2016

Zhou, Z., Belluscio, L., 2012. Coding Odorant Concentration through Activation Timing between the Medial and Lateral Olfactory Bulb. Cell Reports 2, 1143–1150. https://doi.org/10.1016/j.celrep.2012.09.035

Zhu, P., Tian, Y., Chen, Y., Chen, W., Wang, P., Du, L., Wu, C., 2021. Olfactory Optogenetics: Light Illuminates the Chemical Sensing Mechanisms of Biological Olfactory Systems. Biosensors 11, 309. https://doi.org/10.3390/bios11090309